Article

Cancer Cell

Systematic elucidation and pharmacological targeting of tumor-infiltrating regulatory T cell master regulators

Graphical abstract

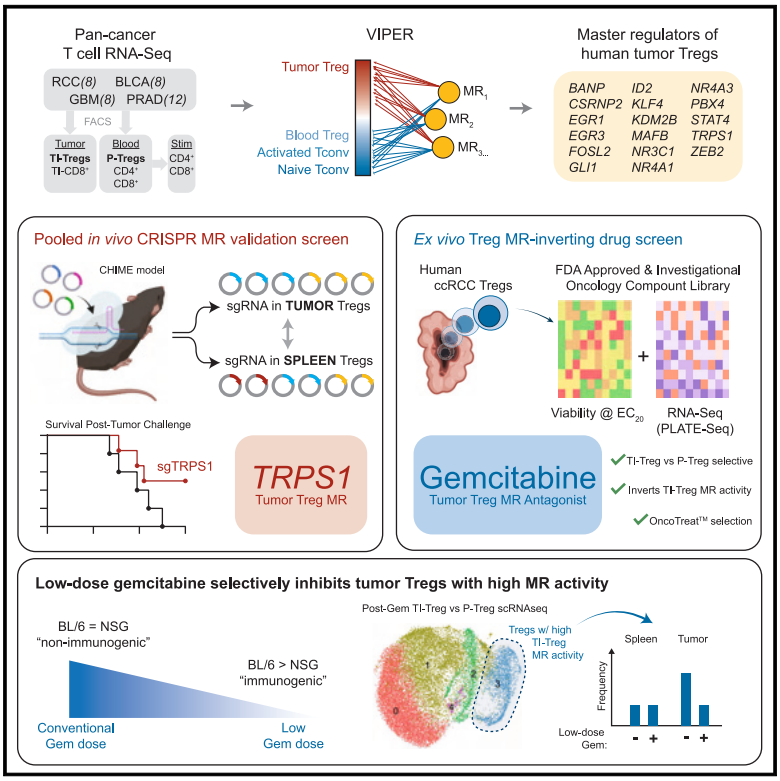

Highlights

- Discovery of proteins specifically active in human TI-Tregs vs. P-Tregs
- TRPS1 validated as the most significant regulator of TI-Treg phenotype
- TRPS1 knockout in hematopoietic cells associates with improved survival in mice
- Drug screen identifies low-dose gemcitabine as differential inhibitor of TI-Tregs

Authors

Aleksandar Obradovic, Casey Ager, Mikko Turunen, ..., Charles Karan, Charles G. Drake, Andrea Califano

Correspondence

ac2248@cumc.columbia.edu

In brief

Obradovic et al. infer and functionally validate a set of master regulator (MR) proteins specifically active in tumor-infiltrating regulatory T cells (TI-Tregs), including TRPS1. Inhibition of TRPS1 improves survival in mouse models. A drug screen revealed that low-dose gemcitabine inhibits TI-Treg MRs and extends survival in immune-competent mice and is synergistic with aPD-1 immunotherapy.

Obradovic et al., 2023, Cancer Cell *41*, 933–949
May 8, 2023
https://doi.org/10.1016/j.ccell.2023.04.003

CellPress

Cancer Cell

CellPress

Article

Systematic elucidation and pharmacological targeting of tumor-infiltrating regulatory T cell master regulators

Aleksandar Obradovic,[1,2,16] Casey Ager,[1,3,16] Mikko Turunen,[2,16] Thomas Nirschl,[4] Mohsen Khosravi-Maharlooei,[1] Alina Iuga,[14] Christopher M. Jackson,[5] Srinivasan Yegnasubramanian,[4] Lorenzo Tomassoni,[2] Ester Calvo Fernandez,[2] Patrick McCann,[9] Meri Rogava,[9] Angelo M. DeMarzo,[4,6,13] Christina M. Kochel,[4] Mohamad Allaf,[6] Trinity Bivalacqua,[6] Michael Lim,[7] Ronald Realubit,[2,8,9] Charles Karan,[2,8,9] Charles G. Drake,[1,4,15] and Andrea Califano[2,8,9,10,11,12,17,*]

[1]Columbia Center for Translational Immunology, Irving Medical Center, New York, NY, USA
[2]Department of Systems Biology, Columbia University Irving Medical Center, New York, NY, USA
[3]Department of Hematology Oncology, Columbia University Irving Medical Center, New York, NY, USA
[4]Department of Oncology, The Johns Hopkins University School of Medicine, Baltimore, MD, USA
[5]Department of Neurosurgery, The Johns Hopkins University School of Medicine, Baltimore, MD, USA
[6]Department of Urology, The Johns Hopkins University School of Medicine, Baltimore, MD, USA
[7]Department of Neurosurgery, Stanford School of Medicine, Palo Alto, CA, USA
[8]J.P. Sulzberger Columbia Genome Center, Columbia University, New York, NY, USA
[9]Herbert Irving Comprehensive Cancer Center, Columbia University Irving Medical Center, New York, NY, USA
[10]Department of Medicine, Columbia University Irving Medical Center, New York, NY, USA
[11]Department of Biochemistry and Molecular Biophysics, Columbia University Irving Medical Center, New York, NY, USA
[12]Department of Biomedical Informatics, Columbia University Irving Medical Center, New York, NY, USA
[13]Department of Pathology, The Johns Hopkins University School of Medicine, Baltimore, MD, USA
[14]Department of Pathology, UNC School of Medicine, Chapel Hill, NC, USA
[15]Present address: Janssen Research and Development, Springhouse, PA, USA
[16]These authors contributed equally
[17]Lead contact
*Correspondence: ac2248@cumc.columbia.edu
https://doi.org/10.1016/j.ccell.2023.04.003

SUMMARY

Due to their immunosuppressive role, tumor-infiltrating regulatory T cells (TI-Tregs) represent attractive immuno-oncology targets. Analysis of TI vs. peripheral Tregs (P-Tregs) from 36 patients, across four malignancies, identified 17 candidate master regulators (MRs) as mechanistic determinants of TI-Treg transcriptional state. Pooled CRISPR-Cas9 screening *in vivo*, using a chimeric hematopoietic stem cell transplant model, confirmed the essentiality of eight MRs in TI-Treg recruitment and/or retention without affecting other T cell subtypes, and targeting one of the most significant MRs (Trps1) by CRISPR KO significantly reduced ectopic tumor growth. Analysis of drugs capable of inverting TI-Treg MR activity identified low-dose gemcitabine as the top prediction. Indeed, gemcitabine treatment inhibited tumor growth in immunocompetent but not immunocompromised allografts, increased anti-PD-1 efficacy, and depleted MR-expressing TI-Tregs *in vivo*. This study provides key insight into Treg signaling, specifically in the context of cancer, and a generalizable strategy to systematically elucidate and target MR proteins in immunosuppressive subpopulations.

INTRODUCTION

To manifest as clinically apparent disease, cancer must evade a complex repertoire of host-protective immune-response mechanisms, the outcome of which is largely determined by the balance of inflammatory (anti-tumor) and tolerogenic (pro-tumor) immune cell function in the tumor microenvironment (TME).[1] By contributing to a tolerogenic TME, the regulatory T cell (Treg) lineage—characterized by activation of the hallmark transcription factor FoxP3—promotes tumor growth and immunotherapy resistance. As such, increased Treg infiltration in the TME correlates with poor prognosis and increased resistance to immune-checkpoint inhibitors across many human malignancies.[2–7] While this makes Tregs attractive therapeutic targets, several factors have prevented clinical translation. First, to avoid severe autoimmunity-mediated toxicity,[2,7] an optimal Treg-directed therapy should target tumor-infiltrating Tregs (TI-Tregs) while sparing peripheral Tregs (P-Tregs). Second, the Treg transcriptional profile broadly recapitulates that of other activated T cells, thus complicating the design of selective targeting strategies that would preserve anti-tumor cytotoxic $CD8^+$ and $CD4^+$ T cell function.[2,8] The majority of current

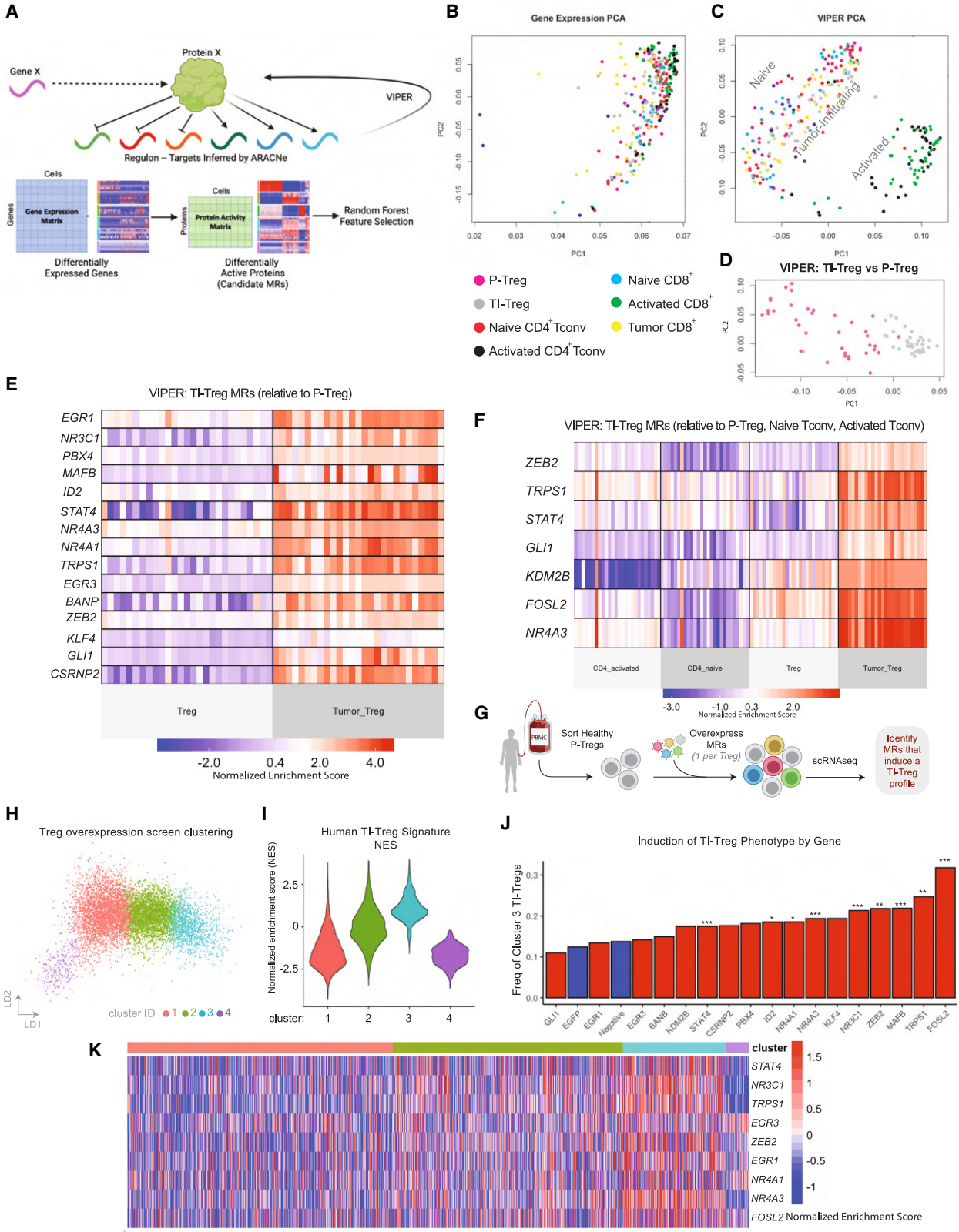

Figure 1. VIPER enables definition of tumor vs. peripheral Treg master regulator signature

(A) Conceptual plot of ARACNe/VIPER protein activity inference process.

(B) Principal component analysis (PCA) plot of gene expression colored by T cell as indicated. P-Treg, peripheral Treg; TI-Treg, tumor-infiltrating Treg.

(legend continued on next page)

Treg-targeting agents do not satisfy these criteria and, although effective in murine models, they have not effectively translated to human patients.[9–11] This highlights the need for elucidating the still elusive causal mechanisms that underlie Treg recruitment, retention, and/or function in the TME, thus leading to identification of more specific TI-Treg vulnerabilities.

To address this challenge, several labs have profiled Tregs isolated from clinical tumor specimens to identify genes differentially expressed in TI- vs. non-TI-Tregs and other T cells. However, differences identified so far have failed to provide tumor infiltration mechanisms that can be successfully targeted pharmacologically. For instance, several studies have successfully validated known TI-Treg biology, including high expression of *IL2RA* (CD25) and *FOXP3* in conjunction with multiple T cell checkpoints (*CTLA4*, *PDCD1* [PD-1], *HAVCR2* [TIM-3], *LAG3*, *TIGIT*), TNF-family receptors (*TNFRSF9* [4-1BB], *TNFRSF18* [GITR], *TNFRSF4* [OX-40]), wound-healing factors (*ENTPD1* [CD39], *IL1RL1* [ST2]), and proliferation programs.[8,12–15] In addition, a number of specific genes enriched in TI-Tregs have been observed across datasets, including *LAYN*, *SAMSN1*, *IL1R2*, *MAGEH1*, *CD177*, and the chemokine receptor *CCR8*. Of these, *CCR8* is one leading candidate, showing preferential protein-level expression in breast cancer[14] and non-small cell lung cancer (NSCLC) TI-Tregs,[16] among others. Monoclonal antibodies targeting *CCR8* and *LAG-3* are currently in multiple clinical trials. However, while *LAG-3* in combination with nivolumab improved progression-free survival in metastatic melanoma by 5 months,[17,18] more recent data suggest *CCR8* may be dispensable for Treg function.[16,19] Thus, despite these advancements, additional efforts are warranted to discover novel potential TI-Treg vulnerabilities via orthogonal approaches.

We have developed methodologies for the assembly and interrogation of lineage-context-specific gene-regulatory networks, including the Algorithm for the Reconstruction of Accurate Cellular Networks (ARACNe)[20] and the Virtual Proteomics by Enriched Regulon Analysis (VIPER) algorithm,[21] respectively (Figure 1A). These have been successful in nominating master regulator (MR) proteins representing mechanistic drivers of both pathophysiologic and transformed transcriptional cell states,[22–24] which have been experimentally validated, including at the single-cell level.[25–27] We thus sought to leverage these methodologies to interrogate a Treg-specific gene-regulatory network with signatures of TI- vs. P-Tregs, to first identify and then validate novel causal MRs driving Treg infiltration into and retainment in the TME.

To generate tumor-agnostic signatures of TI-Treg vs. P-Treg state, we have collected patient-matched transcriptional profiles from multiple T cell subpopulations, isolated from the tumors and peripheral blood of 36 patients by fluorescence-activated cell sorting (FACS), using established antibody panels. We specifically focused on tumor types whose T cell repertoire is not well represented in existing datasets, including prostate adenocarcinoma, bladder cancer, clear cell renal carcinoma, and glioblastoma. With this dataset, we identified transcriptional signatures differentially expressed in TI-Tregs vs. patient-matched peripheral blood Tregs, conventional non-Treg CD4 T cells (Tconv), and $CD8^+$ T cells across a set of highly diverse cancers. We leverage the VIPER algorithm to identify candidate MR proteins whose transcriptional targets are most differentially expressed in TI- vs. P-Tregs and who are thus most likely to comprise the protein module that mechanistically drives and homeostatically maintains the TI-Treg transcriptional state.[21] We have shown that this approach outperforms gene expression-based analyses and compares favorably with single-cell, antibody-based approaches.[25,28,29] Critically, while antibodies measure abundance, this approach measures the *transcriptional activity* of each regulatory protein, i.e., its ability to mechanistically regulate a transcriptional signature of interest.

To further assess whether candidate MR proteins are essential for TI-Treg infiltration and retention in the TME, we leveraged two orthogonal yet complementary methodologies. First, we utilized a CHIME (chimeric immune editing)[30] model to perform a pooled, *in vivo* CRISPR-Cas9 screen to assess whether targeting of the candidate MRs by CRISPR knockout (KO) would deplete TI-Tregs, without affecting P-Tregs, thus confirming their mechanistic role in mediating naive Treg recruitment and/or TI-Treg retention in the TME. Second, we performed a systematic drug screen where patient-derived TI-Tregs were expanded *ex vivo* and their response to perturbations with a large compound library was assessed by RNA-sequencing (RNA-seq) profiling (“perturbational profiles”). Candidate MR-inverter compounds—capable of specifically inverting the activity of the TI-Treg MRs—were nominated using the NY/CA Department of Health-approved, CLIA-compliant OncoTreat algorithm[31] and validated. A critical value of this approach is its highly generalizable nature and potential for rapid translation of mechanism-based therapeutic strategies

(C) PCA plot of VIPER-inferred protein activity, colored as in (B), showing spatial separation of T cell subtypes.
(D) PCA plot of VIPER-inferred protein activity separating TI-Tregs and P-Tregs only, colored as in (B) and (C).
(E) Heatmap of VIPER protein activity for master regulators identified by random forest feature selection as best distinguishing TI-Tregs vs. P-Tregs.
(F) Heatmap of VIPER protein activity for master regulators identified by random forest feature selection as best distinguishing TI-Tregs vs. all peripheral controls (P-Tregs, naive Tconv, activated Tconv).
(G) Experimental design of overexpression screen, where the predicted TI-Treg MR ORFs (17 in total) are individually overexpressed in sorted P-Tregs and then 7 days later profiled by scRNA-seq.
(H) Linear discriminant analysis (LDA) plot showing unsupervised clustering of Treg phenotypes by scRNA-seq from experiment described in (E).
(I) Violin plot of cell-by-cell gene set enrichment analysis (GSEA) of 27 TI-Treg MRs for cells shown in (F), such that cluster 3 cells are significantly enriched for TI-Treg signature.
(J) Bar plot of cluster 3 frequencies grouped by overexpressed gene, where negative controls (no gene overexpressed and *EGFP* overexpressed) are colored blue and candidate MRs are colored red. ***$p < 0.001$ relative to negative control, **$p < 0.01$, *$p < 0.05$, by Bonferroni-adjusted Fisher’s exact test.
(K) Heatmap of protein activity for inferred TI-Treg MR proteins at the single-cell level, in the experiment described in (G)–(J), grouped by cluster as in (H) and (I). Shows co-upregulation of entire MR module in every cell from cluster 3, regardless of which individual MR was overexpressed.
See also Figures S1 and S2.

Table 1. GSEA of TI- vs. P-Treg MR proteins between tumor contexts, Bonferroni corrected

Candidate MR	Differentially active protein	p	Candidate MR	Differentially active protein	p
GBM	PRAD	4.70E−07	PRAD	GBM	1.30E−11
GBM	KIRC	7.20E−07	KIRC	GBM	6.90E−11
GBM	BLCA	2.10E−05	BLCA	GBM	1.10E−06
PRAD	KIRC	3.40E−11	KIRC	PRAD	2.20E−04
PRAD	BLCA	8.10E−08	BLCA	PRAD	2.30E−07
KIRC	BLCA	2.10E−05	BLCA	KIRC	1.30E−08

for modulating TI-Treg infiltration and retention to the TME, thus potentiating immunotherapy.

RESULTS

Isolating tumor- (TI-Tregs) vs. blood-derived (P-Tregs) regulatory T cells

Tumor and patient-matched peripheral blood tissues were collected from 36 individuals, including 8 glioblastoma (GBM), 8 bladder adenocarcinoma (BLCA), 8 clear cell renal carcinoma (KIRC), and 12 prostate adenocarcinoma (PRAD) patients. Multiple T cell lineages were freshly sorted from each patient by antibody-based flow cytometry, including TI-Tregs, P-Tregs, peripheral blood CD4 T cells, and both tumor-infiltrating and peripheral blood $CD8^+$ T cells; see Figure S1 for sorting strategies. Purity was assessed by flow and exceeded 95% for each population (Figures S1A–S1E). To provide additional controls for T cell activation, patient-matched flow-sorted naive peripheral (i.e., blood-derived) $CD4^+$ and $CD8^+$ T cells from each of the 36 patients were stimulated for 72 h with anti-CD3/anti-CD28 beads. Total RNA was purified from each of these seven distinct T cell subpopulations, and RNA-seq profiles were generated by Illumina sequencing, for a total of 236 distinct RNA-seq profiles.

Nominating candidate master regulators of the TI-Treg transcriptional state

To maximize biological signal to noise, we applied protein activity inference to the sorted RNA-seq profiles (Figure 1A). Gene expression-based cluster analysis produced poor stratification of different T cell subtypes (Figure 1B). This is likely due to the inherent noise in transcriptional data, as RNA counts represent a proxy for the biological activity of proteins that determine cell state. After a protein is expressed, its activity is manifested only when it is effectively post-translationally modified, is translated to the appropriate subcellular compartment, and forms complexes with critical cognate binding partners. By inferring a network of the downstream transcriptional targets for each transcription factor (TF), co-transcription factor (CoTF), and signaling protein using the ARACNe algorithm, we may effectively assess the activity of upstream proteins from the expression patterns of their targets using VIPER. Having shown that protein activity-based cluster analysis consistently outperforms expression-based analyses,[24,25] we proceeded to generate a TI-Treg-specific gene-regulatory network by analyzing the 236 T cell-derived profiles using AP-ARACNe[32]—the latest version of the ARACNe algorithm[20]—followed by VIPER-based measurement of differential protein activity for each sample against the average of all samples (STAR Methods), as previously described in multiple publications.[21] Activity-based cluster analysis showed clear separation of naive and activated T cells by 2D principal-component analysis (PCA), with tumor-infiltrating cells comprising a distinct cluster (Figure 1C). Intriguingly, neither gene expression nor protein activity could stratify TI-Treg samples by tumor type, suggesting a relatively tumor-agnostic transcriptional state. However, while gene expression could not differentiate between TI- and P-Tregs in PCA space, MR analysis nearly perfectly stratified the two subpopulations (Figure 1D).

Consistent with these findings, a random forest classifier for TI- vs. P-Treg state, independently trained on the statistically significant MRs ($p \leq 10^{-3}$), as assessed independently from samples of each tumor type (e.g., using GBM samples only), could precisely classify TI- vs. P-Tregs across all other tumor types (e.g., PRAD, BLCA, and KIRC), producing a perfect pairwise area under the receiver operating curve metric (AUROC = 1.0) for all comparisons. Consistently, there was highly significant enrichment (ranging from $p = 10^{-4}$ to $p = 10^{-11}$) of candidate MRs inferred from a single tumor type—based on VIPER analysis of genes differentially expressed in tumor patient-specific TI- vs. P-Tregs ($p \leq 10^{-3}$)—in proteins differentially active in TI- vs. P-Tregs from each other tumor type, by gene set enrichment analysis (GSEA)[33] (Table 1).

To select the most discriminative candidate MRs among those differentially active in TI-Tregs vs. other T cell populations—including P-Tregs, naive CD4 T cells, and activated CD4 T cells—we used the random forest algorithm (see STAR Methods). Specifically, this analysis selected the minimal number of features (i.e., candidate MRs, starting from the most statistically significant one) that maximized the ratio between the AUROC from a Monte Carlo cross-validation (MCCV) analysis and the null hypothesis (i.e., equal number of randomly selected transcriptional regulators) (Figures 1E and 1F). The analysis yielded 15 candidate MR proteins significantly differentially active in TI- vs. P-Tregs, shown in Figure 1E (AUROC = 0.982 for TI- vs. P-Treg classification by MCCV; Figure S2A). In addition, seven candidate MRs were found to optimally classify TI-Tregs vs. other control subpopulations, shown in Figure 1F (AUROC = 0.988 by MCCV; Figure S2A). Of these, only 2 were not included in the previous 15, yielding a total of 17 unique candidate MRs of Treg tumor infiltration, namely *EGR1*, *NR3C1*, *PBX4*, *MAFB*, *ID2*, *STAT4*, *NR4A3*, *NR4A1*, *TRPS1*, *EGR3*, *BANP*, *ZEB2*, *KLF4*, *GLI1*, *CSRNP2*, *KDM2B*, and *FOSL2*. Of these, the *NR4A* family of transcription factors,[34] as well as *FOSL2*,[35] were previously reported as upstream regulators of *FOXP3* expression in Tregs; the glucocorticoid receptor *NR3C1* was shown to have Treg-specific function[36]; and *EGR3* was reported as a negative regulator of T cell activation.[37]

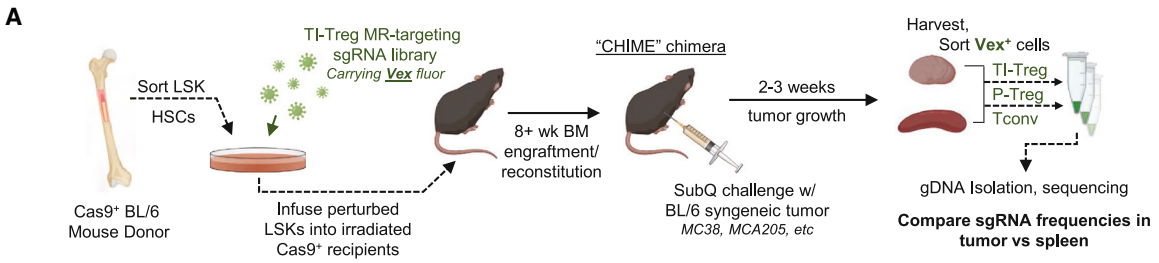

B

sgRNA library target genes

TI-Treg MRs		Neg. Controls	Pos. Controls
Banp	*Mafb*	*Scx*	*Cd4*
Csrnp2	*Nr3c1*	*E2f7*	*Cdk1*
Egr1	*Nr4a1*	*Nr6a1*	*Foxp3*
Egr3	*Nr4a3*	*Prdm8*	*Plk1*
Fosl2	*Pbx4*	*Srfbp1*	
Gli1	*Stat4*	*Nhlh1*	
Id2	*Trps1*		
Klf4	*Zeb2*		

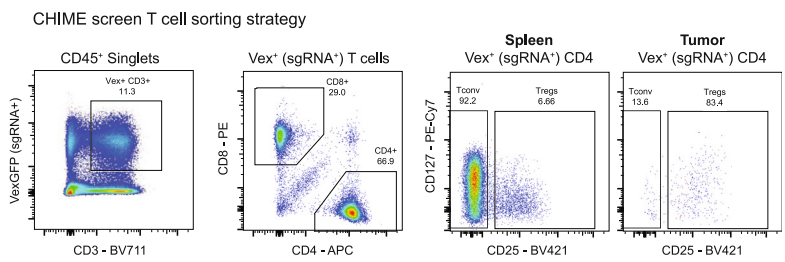

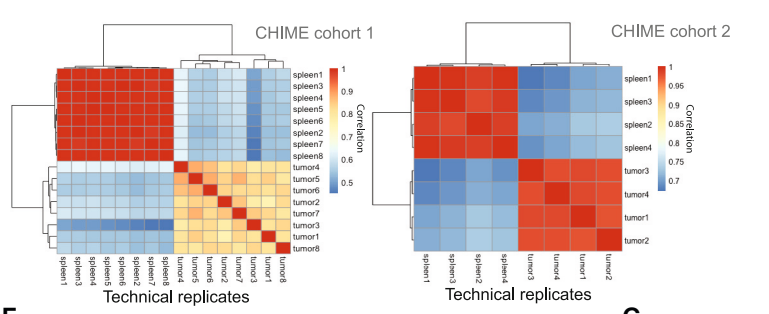

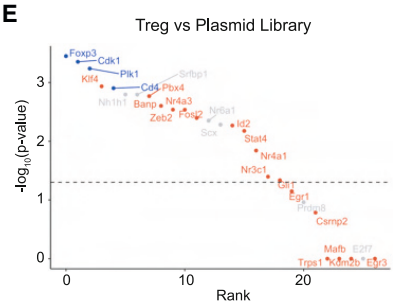

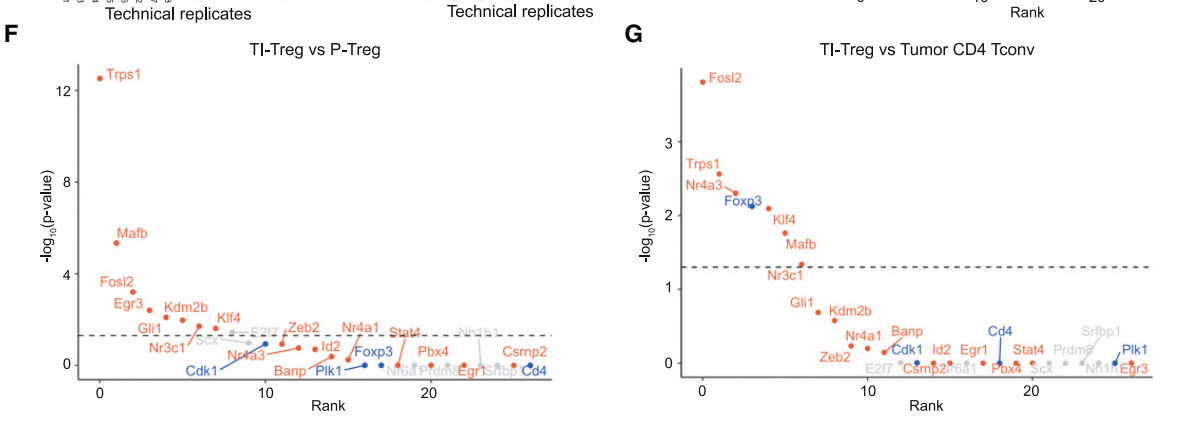

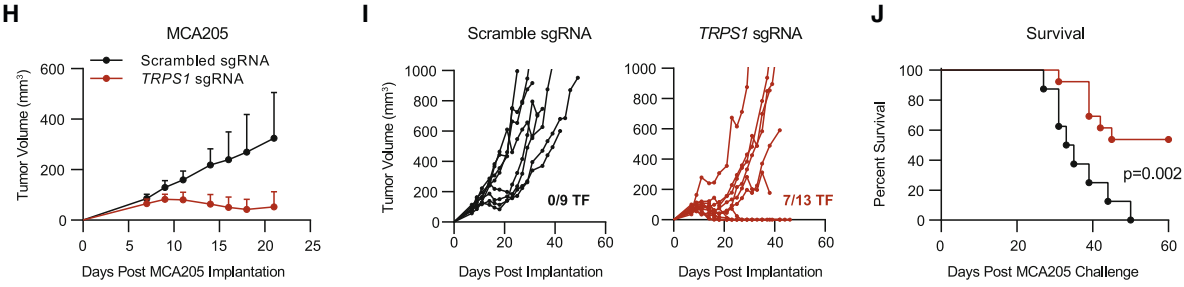

Figure 2. Chimeric immune editing mouse model enables validation of Treg tumor-infiltration master regulators

(A) Experimental design for *in vivo* CRISPR KO validation of TI-Treg MRs.

(B) List of sgRNAs targeting 17 TI-Treg MRs, 6 negative control genes, and 4 positive control genes.

(legend continued on next page)

However, none were previously reported as causal regulators of Treg tumor infiltration and none were significantly differentially expressed at the RNA level in TI-Tregs in our dataset.

Candidate MR validation by *in vitro* overexpression assay

To further assess whether candidate MRs play a mechanistic role in controlling Treg state, we tested whether ectopic expression of any of the 17 computationally predicted individual TI-Treg MRs was sufficient to convert naive Tregs to a TI-Treg-like state. For this, we performed an arrayed (one open reading frame [ORF]/well) overexpression screen in human P-Tregs, where we lentivirally overexpressed each of the 17 predicted TI-Treg MR ORFs, with one MR overexpressed per cell (Figure 1G). EGFP-ORF and non-transduced naive Tregs were used as assay negative controls. Seven days after the lentiviral transductions, we performed single-cell RNA-seq (scRNA-seq) profiling of the resulting cells.

We performed unsupervised clustering of Treg phenotypes for all the single cells within our assay (Figure 1H). In this analysis, one cluster (C3) emerged as significantly enriched in the TI-Treg gene signature (the set of 17 genes identified as TI-Treg MRs in our analysis above) by GSEA ($p < 0.05$) (Figure 1I). Confirming our predictions, within this C3/TI-Treg cluster, the ORFs of 11/17 candidate MRs were significantly enriched, meaning that individually overexpressing any of these 11 MRs caused a concurrent change in the entire MR module and overall shift in transcriptional signature closer to the TI-Treg cell state. The strongest enrichments were seen with overexpression of *FOSL2* (32%, $p = 1.3 \times 10^{-15}$) and *TRPS1* (25%, $p = 0.0062$), compared with only 13% of Tregs harboring the negative control that spontaneously acquired this phenotype via anti-CD3/anti-CD28 bead-based stimulation in culture (Figure 1J). Critically, the entire set of TI-Treg MRs was concurrently active in C3 at a single-cell level, regardless of which one had been overexpressed (Figure 1K). This result shows that several of the VIPER-inferred MRs play a causal, mechanistic role in reprogramming Treg cell state and suggests that activation or inhibition of the entire MR module may induce even more significant effects.

Candidate MR validation by *in vivo* pooled CRISPR KO screen

To functionally validate whether the computationally predicted MRs are essential for TI-Treg recruitment to and/or retention in the TME, we performed an *in vivo* pooled CRISPR KO screen using the CHIME system.[30] Briefly, we sorted $Lin^{-}Sca\text{-}1^{+}c\text{-}Kit^{-}$ cells enriched for hematopoietic stem cells (HSCs) from constitutive Cas9-expressing mice and lentivirally transduced them with an sgRNA library targeting 34 genes, for a total of 102 guides (i.e., 3 guides/gene). Target genes included the 17 MRs described above, 6 randomly selected negative control genes with low baseline expression in T cells, and 4 positive controls known to be essential in Tregs or in all cells, including *Cd4* (CD4 T cell essential), *Foxp3* (Treg essential), and *Plk1* and *Cdk1* (globally essential) (Figures 2A and 2B). Guides were cloned in the pXPR_053 vector (see STAR Methods), which includes a VexGFP (Vex) fluorophore for transduced cell selection. HSCs were then implanted into irradiated Cas9-tolerized recipients, allowing the immune system to reconstitute *de novo* over at least 10 weeks, such that all Vex^{+} immune-lineage cells, including Tregs, harbored co-expression of a given guide RNA and Cas9. Syngeneic MC38 colon carcinoma tumors, chosen for their well-established reliance on an intact TI-Treg compartment for *in vivo* growth,[38] were implanted and allowed to grow for approximately 3 weeks. Finally, Vex^{+} Tregs as well as CD4 Tconv cells were flow-sorted from the tumor and spleen (control) of each mouse (Figure 2C). The latter was selected as an effective reservoir of P-Tregs such that differential sgRNA barcode abundance could be compared in TI-Tregs vs. spleen P-Tregs. Since this screen was intended for validation rather than discovery, measures were taken to minimize the false-positive rate, such that negative controls consisted of randomly sampled non-MR genes rather than non-targeting guides, and guide frequencies were compared by permutation-based non-parametric empirical p value.

Upon engraftment and reconstitution of the hematopoietic system, roughly 25%–40% of immune cells expressed VexGFP fluorophore, indicating that most transduced Treg cells harbored a single sgRNA perturbation (Figure S2B). To assess reproducibility, two separate CHIME chimera cohorts were implanted with syngeneic MC38 tumors, the second being implanted with $Lin^{-}Sca\text{-}1^{+}c\text{-}Kit^{-}$ HSCs from the bone marrow of the first. Tumors in the second cohort were grown for 18 days before $CD4^{+}CD25^{+}$ Tregs and $CD4^{+}CD25^{-}$ Tconv cells were sorted from the tumor and spleen of each animal (Figure 2C) and sequenced to assess differences in sgRNA representation. Confirming reproducibility, differential representation of individual sgRNAs in TI- vs. P-Tregs was significantly correlated in the two cohorts ($p < 0.01$; Figure 2D). All four positive control genes were depleted as expected in Tregs relative

(C) Representative flow cytometry gating for Vex^{+} CRISPR-transduced Tregs, CD4 non-Tregs, and $CD8^{+}$ T cells in spleen and tumor.
(D) Correlation of sgDNA frequency distribution between replicates of spleen and tumor Tregs in experimental cohorts 1 (left) and 2 (right). Within each cohort, samples of spleen and tumor represent technical replicates of pooled tissue, while the two cohorts are themselves independent biological replicate experiments.
(E) Plot of −log10(Bonferroni-corrected p value) vs. p-value rank for gene depletion in P-Tregs vs. input plasmid library, where blue indicates positive control genes, red indicates candidate TI-Treg MRs, and gray indicates negative controls. Horizontal dashed line indicates $p = 0.05$.
(F) Plot of −log10(Bonferroni-corrected p value) vs. p-value rank for gene depletion in TI-Tregs vs. P-Tregs, with color coding and dashed line as in (E).
(G) Plot of −log10(Bonferroni-corrected p value) vs. p-value rank for gene depletion in TI-Tregs vs. tumor-infiltrating CD4 non-Tregs, with color coding and dashed line as in (E).
(H) Tumor growth curves of MCA205 (8×10^{5} implanted subcutaneously) in mice bearing single gene *Trps1* sgRNAs (red) vs. scrambled sgRNAs (black) in the hematopoietic lineage. Data are shown as the average across mice.
(I) Individual growth curves of mice in (H), with numbers of tumor-free mice (TF) noted.
(J) Kaplan-Meier plot for overall survival time of mice in (I), showing significant difference in tumor growth ($p = 0.002$ by log-rank test).
See also Figure S2.

to the starting plasmid library (Figure 2E). Of the 17 candidate MR proteins, 8 presented significantly depleted sgRNAs in TI-Tregs vs. spleen P-Tregs—including *Trps1*, *Mafb*, *Fosl2*, *Egr3*, *Gli1*, *Kdm2b*, *Nr3c1*, and *Klf4* (Figure 2F)—suggesting a causal role in Treg tumor infiltration and/or retention in the TME. Frequency distribution of sgRNAs in P-Tregs and TI-Tregs for both experimental cohorts is shown in Figures S2E and S2F. Critically, five of the eight validated MR candidates—including *Trps1*, *Mafb*, *Fosl2*, *Klf4*, and *Nr3c1*—were also significantly depleted in TI-Tregs relative to tumor CD4 Tconv (Figure 2G), thus supporting their TI-Treg-specific rather than T cell-specific function. Of note, the positive control *Foxp3*, which is Treg essential but not $CD4^+$ Tconv essential, was significantly depleted in Tregs relative to $CD4^+$ Tconv (Figure 2G). The most statistically significant protein emerging from the comparison of TI-Tregs vs. P-Tregs was *Trps1* ($p = 2.21 \times 10^{-13}$), a protein with previously unknown function in T cells, including Tregs (Figure 2F).

CRISPR KO targeting of Trps1 in hematopoietic lineages inhibits tumor growth

Based on these findings, we further interrogated the phenotype induced by CRISPR KO targeting of Trps1, the MR whose guide RNAs were most significantly depleted in TI-Tregs vs. P-Tregs and whose expression was sufficient to induce the TI-Treg cell state in naive human P-Tregs. Specifically, two guide RNAs targeting the encoding gene, *Tprs1*, were transduced into Cas9-expressing $Lin^-Sca1^+c\text{-}Kit^+$ cells (LSKs) that were then used to reconstitute the lethally irradiated bone marrow of 13 chimeras across two experimental cohorts. As negative controls, we reconstituted the bone marrow of nine mice with LSKs transduced with two non-targeting (scramble) guides. To assess the tumor-agnostic nature of TI-Treg infiltration by MRs, we implanted these mice with a complementary syngeneic tumor model, MCA205, representing a well-studied, poorly immunogenic fibrosarcoma.[39] In initial studies, we found that the MC38 tumor model ultimately experiences spontaneous tumor regression in CHIME mice on longer timescales even with non-targeting guides, motivating the use of MCA205 as an orthogonal and more immune-resistant tumor and a higher bar for survival effects of targeting *Trps1*. Confirming the MR's functional relevance, we observed a significant survival advantage in sgTrps1 mice vs. sgControl mice. In particular, we observed spontaneous, durable tumor rejection (>60 days) in 7 of the 13 sgTrps1 (54%), but none of the sgControl animals (Figures 2H and 2I), and an overall survival comparison p value of 0.002 (Figure 2J).

In conjunction with the above-described CRISPR KO and overexpression screens, these data suggest that TRPS1 activity is essential for Tregs to acquire and maintain their infiltrating, immunosuppressive potential in the TME. Supporting the tumor-context-specific role for TRPS1, we observed no statistically significant decrease in *ex vivo* suppressive capacity of Tregs containing Trps1-sgRNAs vs. scramble sgRNAs (Figure S2C) and no consistent signs of autoimmunity or immunopathology across peripheral tissues (skin, colon, small intestine, liver, and kidney) in these mice upon histological review by a trained pathologist blinded to sample group (Figure S2D). These data support that the observed immunomodulatory effects of sgTrps1 KO on Tregs are restricted to the TME.

Systematic identification of TI-Treg-specific MR-inverter drugs

To identify drugs that could specifically inhibit Treg infiltration/retention in the TME by targeting the TI-Treg MR proteins identified by our study, such as TRPS1, we generated RNA-seq profiles of sorted human TI-Tregs at 24 h following treatment with a library of clinically relevant compounds. To reduce study complexity and cost, we first assessed the effects of a library of 1,554 FDA-approved and investigational compounds on human-derived P-Treg viability at a single, relatively large concentration (5 μM). For this screen, human P-Tregs were flow-sorted, expanded *ex vivo*, and treated with drugs in a 96-well plate format (Figure 3A). We then selected 195 bioactive compounds that inhibited P-Treg viability ≥60% (Figure 3B). To further reduce the number of candidate drugs, we then generated 10-point drug-response curves to identify the 48-h EC_{20} concentration of the 195 compounds and selected the 86 compounds with the lowest EC_{20} for efficient perturbational profile analysis in a 96-well format, also considering inclusion of vehicle controls (DMSO). As previously reported,[40,41] the 48-h EC_{20} (maximum sublethal) concentration was selected to effectively assess each drug's mechanism of action at 24 h, while reducing confounding effects arising from activation of cell stress or death pathways. Finally, the 48-h EC_{20} concentration of each compound was used to perturb TI-Tregs flow-sorted from a treatment-naive human clear cell carcinoma specimen and expanded, *ex vivo*, into 96-well plates, followed by RNA-seq profiling using the fully automated PLATE-seq technology.[40,41]

Viability data, as well as perturbational RNA-seq profiles of TI-Tregs, were collected (Figures 3C and 3D). Based on the differential protein activity signature in drug- vs. vehicle control-treated TI-Tregs, we identified compounds capable of inducing statistically significant inactivation of TI-Treg-specific MR proteins using the OncoTreat algorithm.[31] From this analysis, 32 compounds were nominated as statistically significant inhibitors of the 17-MR TI-Treg signature ($p < 1 \times 10^{-5}$), which includes TRPS1 (Figure S3A). Of these, seven preferentially depleted TI-Treg vs. P-Treg viability *in vitro* (Figures 3C and 3D) and were also predicted by OncoTreat to inhibit the TI-Treg vs. P-Treg MR signature—on a patient-by-patient basis—across all tumor types and nearly all patients (Figure 3E). Of these, three (i.e., gemcitabine, triapine, and floxuridine) were among the seven most significant TI-Treg MR activity inhibitors—as predicted across all 36 patients in the study (Figure S3B)—and also among the top six inducing the most significant differential TI- vs. P-Treg viability reduction *in vitro* (Figure 3C).

Dose-response curves of these three drugs revealed that only gemcitabine had a gradual dose-dependent effect on Treg viability reduction, as a function of its concentration, while the other two had sharp elbows consistent with a threshold effect that would challenge appropriate concentration selection for *in vivo* studies (Figures S4A–S4C). In addition, floxuridine had cytostatic rather than cytotoxic activity, even at high concentration, and neither floxuridine nor triapine was confirmed to affect overall survival in the MC38 mouse model (Figure S4D). Surprisingly, gemcitabine was predicted to drive TI- to P-Treg signature conversion, including TRPS1 inhibition, at a remarkably low concentration *in vitro* (10 nM) (Figure S3B), which is much lower than

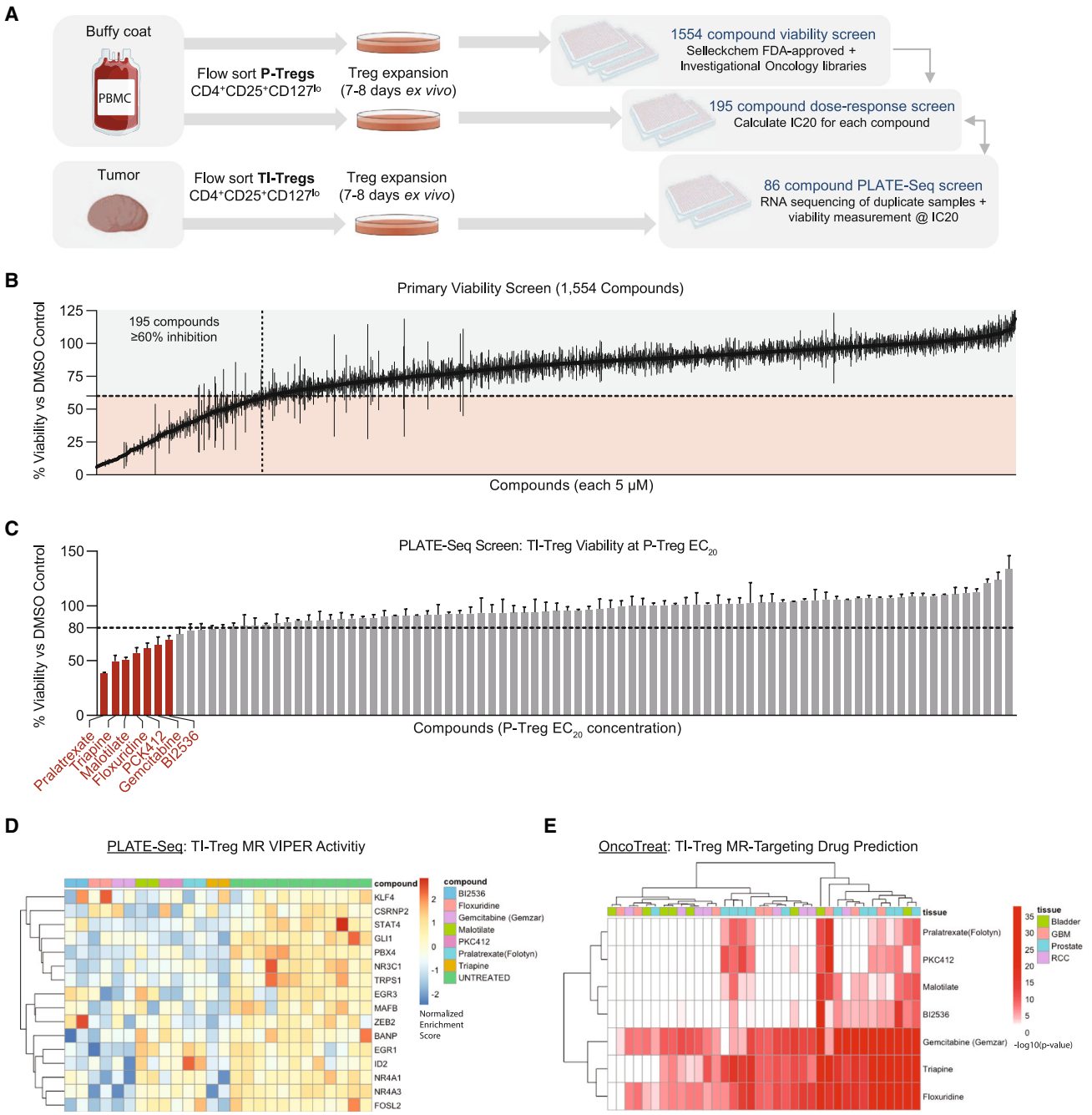

Figure 3. High-throughput drug screening platform identifies potential drug candidates with tumor-Treg-directed toxicity

(A) Experimental design of high-throughput Treg-directed drug toxicity screen.

(B) Results from initial set of 1,554 FDA-approved and investigational oncology compounds screened at a single dose for peripheral Treg growth inhibition, with 195 compounds showing >60% inhibition at 5 μM.

(C) Viability results of the PLATE-seq screen, where human tumor Tregs were assessed for growth inhibition on sorted tumor Tregs at peripheral-Treg EC_{20} dose, resulting in seven drugs with higher toxicity in TI-Tregs relative to P-Tregs. Data are shown as percentage viability for each drug vs. DMSO control.

(D) Heatmap of VIPER protein activity for tumor vs. peripheral Treg MRs defined in Figures 1E and 1F comparing transcriptional effect of drugs in (C) vs. untreated control, with downregulation of nearly all identified MRs by these drugs.

(E) Patient-by-patient drug predictions according to inversion of patient tumor Treg vs. peripheral Treg protein activity signature by drug-treatment protein activity signature. Each drug predicted to invert tumor Treg signature with −log10(Bonferroni-corrected p value) <0.01 in a particular patient is colored red. Patients are grouped by tumor type. The plot is subset to show only drugs identified by tumor Treg growth screen in (C), with columns colored by tumor type and clustered by unsupervised hierarchical clustering.

See also Figures S3 and S4.

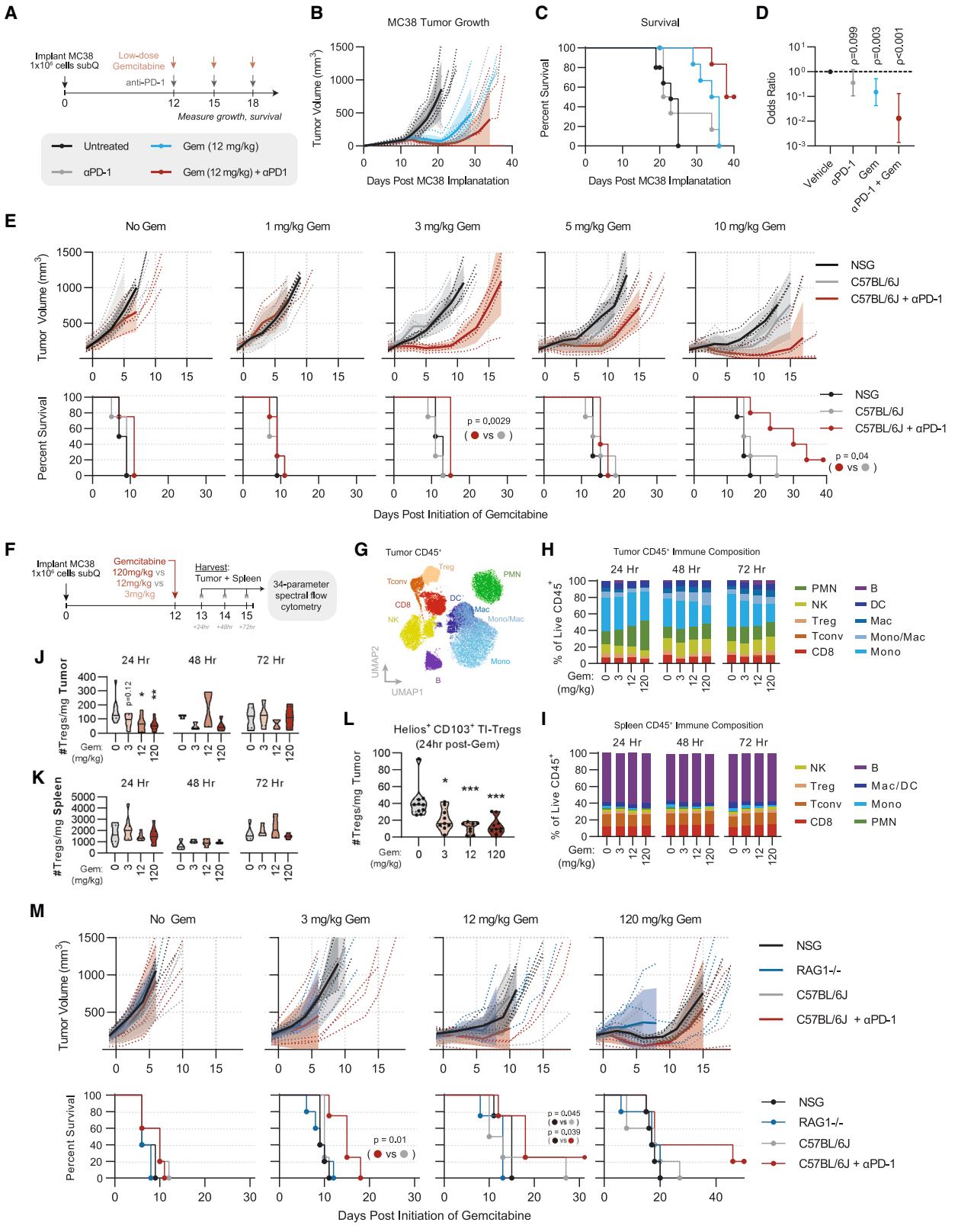

(legend on next page)

the concentration achieved at clinical doses. As a result, we focused on this drug for *in vivo* validation purposes.

Immunomodulatory effects of low-dose gemcitabine contribute to its efficacy and synergy with immunotherapy

To validate the preferential TI-Treg targeting of gemcitabine *in vivo*, we implanted C57BL/6J mice subcutaneously with MC38 syngeneic tumors and initiated therapy 12 days later, a "late stage" of growth when MC38 tumors are resistant to anti-PD-1 immunotherapy.[42] Low-dose gemcitabine was administered intraperitoneally (i.p.) on days 12, 15, and 18, at 12 mg/kg, representing ~1/10 of the lowest conventional clinically relevant dose in mice (120 mg/kg).[43,44] In an additional treatment arm, mice received gemcitabine in combination with anti-PD-1 administered i.p. on days 12, 15, and 18 (Figure 4A). As expected, late-stage MC38 tumors failed to respond to anti-PD-1. However, single-agent low-dose gemcitabine temporarily controlled MC38 progression, conferring a significant reduction in growth kinetics ($p = 0.003$) and prolongation of survival ($p = 0.006$) relative to vehicle-treated mice (Figures 4A–4D). In combination, low-dose gemcitabine sensitized late-stage MC38 tumors to anti-PD-1, achieving complete responses in 50% of animals, translating to a significant survival advantage compared with gemcitabine alone ($p = 0.009$) (Figures 4A–4D).

To assess whether low-dose gemcitabine effects were immune mediated, we performed parallel dose titrations in immune-competent C57BL/6J mice and severely immune-deficient NSG (NOD.Cg-Prkdc^{scid} Il2rg^{tm1Wjl}/SzJ) mice lacking both innate and adaptive immunity. At a clinically relevant dose (120 mg/kg)[43,44] gemcitabine inhibited tumor growth in both C57BL/6J and NSG mice relative to vehicle control ($p < 0.001$, by Cox regression analysis) with no significant difference between the two strains ($p = 0.19$; Figures S4E and S4F). We found that efficacy was lost in both strains within the range of 12 to 1.2 mg/kg, with a modest advantage in C57BL/6 mice at 12 mg/kg ($p = 0.012$) and a trending advantage at 1.2 mg/kg ($p = 0.09$; Figure S4F). Although modest, these data are in line with previous observations in immunodeficient nude mice,[45] suggesting the therapeutic effects of low-dose gemcitabine are at least in part due to its immunomodulatory properties.

To test whether immune-dependent activity could be observed in this range of concentrations, we dosed cohorts of mice with 1–10 mg/kg gemcitabine, with an additional cohort of C57BL/6J mice receiving anti-PD-1 in combination. We found that doses as low as 3 mg/kg, which lack any activity in NSG mice ($p = 0.84$), reveal sensitivity to anti-PD-1 via tumor growth kinetic reduction ($p = 0.01$) and enhanced survival ($p = 0.0029$) in the combination group (Figure 4E). As above, the benefit observed in C57BL/6J vs. NSG strains is modest ($p = 0.253$); however, in immune-competent mice, this dose is sufficient to augment anti-PD-1 therapy to achieve curative responses and a significant enhancement of survival relative to gemcitabine or anti-PD-1 alone ($p = 0.048$, $p = 0.005$, respectively; Figures 4A–4D). Taken together, these data show that low-dose gemcitabine is in part dependent upon host immunity and effectively sensitizes anti-PD-1-resistant MC38 tumors to immune-checkpoint blockade therapy.

Low-dose gemcitabine selectively targets TI-Tregs *in vivo*

To better understand the immunomodulatory effects of low-dose gemcitabine and evaluate whether they are restricted to TI-Tregs, we performed high-parameter flow cytometry analysis of tumors and spleens from MC38 tumor-bearing C57BL/6J mice post-gemcitabine treatment, utilizing a 34-parameter spectral flow cytometry panel. We evaluated tissues from mice receiving high-dose gemcitabine (120 mg/kg), low-dose gemcitabine (12 mg/kg), or a minimally effective dose of gemcitabine (3 mg/kg), as well as vehicle-treated controls, and evaluated immediate effects 24 h post-treatment, as well as delayed/secondary effects at 48 and 72 h post-treatment (Figures 4F–4I and S5A–S5C). Although gemcitabine elicits compositional changes throughout the CD45$^+$ infiltrate (Figures 4G and 4H), Tregs are the only immune subset significantly reduced in absolute number in tumors by low-dose gemcitabine (Figures 4J and S5D). Splenic Tregs are not reduced in number by gemcitabine at any dose, confirming that the inhibitory effects of low-dose gemcitabine are restricted to Tregs infiltrating the tumor (Figure 4K). Our data suggest that this tumor-specific effect is not solely based on greater Treg proliferation within tumors, as gemcitabine inhibited Ki67 staining in Tregs in both the tumor and the

Figure 4. Low-dose gemcitabine is immunogenic and potentiates anti-PD-1 therapy

(A) Schematic of *in vivo* validation studies. Experiment consists of six mice per group.

(B–D) Tumor growth curves for each treatment group (B), Kaplan-Meier survival curves (C), and forest plot (D) showing the result of multiple Cox regression assessing the treatment effect on time-to-death for each of the treatments described in (A). Hazard ratios are shown with 95% confidence interval and p value. Results are representative of two independent experiments.

(E) Tumor growth and Kaplan-Meier survival curves of NSG mice, C57BL/6J mice, and C57BL/6J mice exposed to anti-PD-1 therapy receiving the indicated dose of gemcitabine between 1 and 10 mg/kg. Statistical significance for survival was calculated by Mantel-Cox log-rank test.

(F) Experimental design of flow cytometry experiment.

(G) Overall flow cytometry clustering of tumor immune cells.

(H) Stacked bar plot of frequencies for clusters shown in (G), split by time point and gemcitabine dose, for tumor.

(I) Stacked bar plot of frequencies for clusters shown in (G), split by time point and gemcitabine dose, for spleen.

(J) Violin plot of Treg absolute numbers per milligram of tumor, split by time point and gemcitabine treatment dose; *$p < 0.05$ and **$p < 0.01$ by two-way ANOVA with multiple testing correction.

(K) Violin plot of Treg absolute numbers per milligram of spleen, split by time point and gemcitabine treatment dose.

(L) Violin plot of Helios$^+$CD103$^+$ TI-Treg cluster absolute numbers per milligram tumor 24 h post-treatment, split by gemcitabine dose.

(M) Tumor growth and Kaplan-Meier survival curves of NSG mice, RAG1-KO mice, C57BL/6J mice, and C57BL/6J mice exposed to anti-PD-1 therapy receiving the indicated dose of gemcitabine between 0 and 120 mg/kg. Statistical significance for survival was calculated by Wilcoxon test. All significant pairwise comparisons ($p < 0.05$) are shown.

See also Figures S4 and S5.

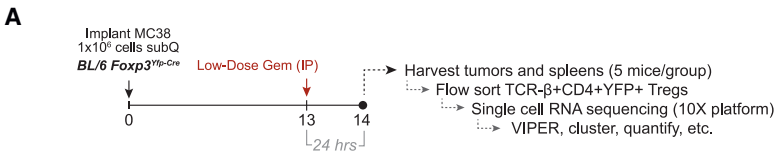

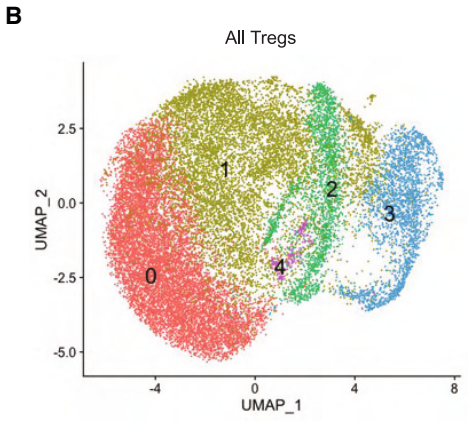

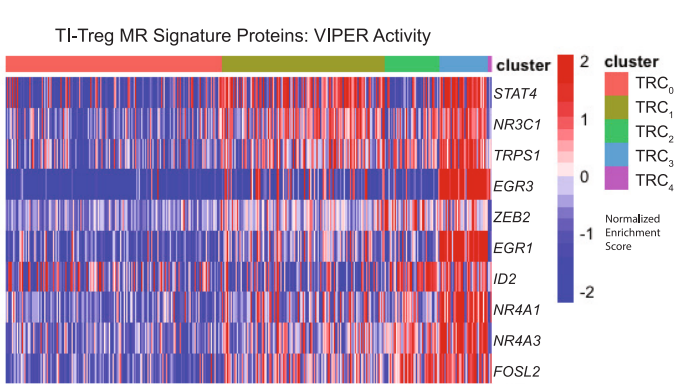

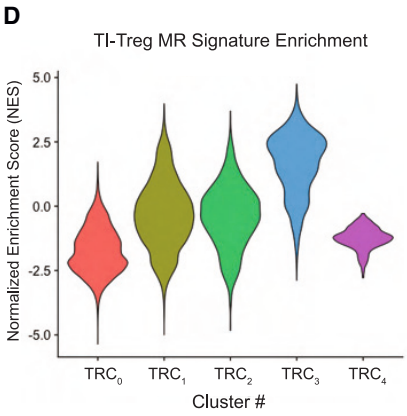

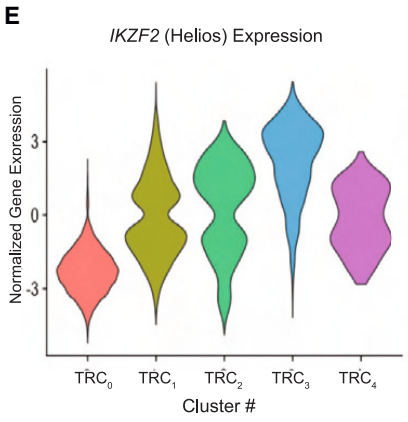

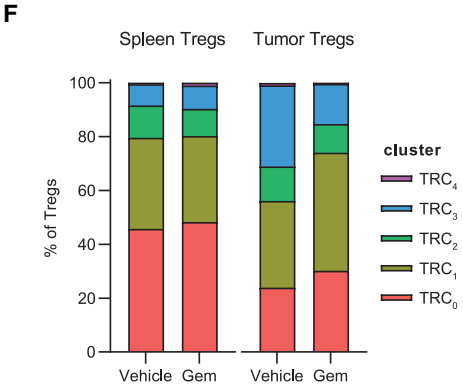

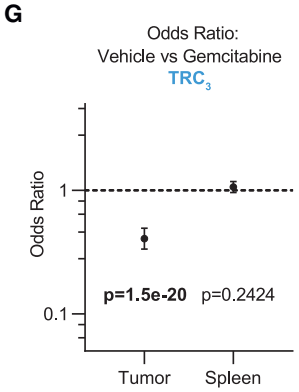

(legend on next page)

periphery (Figures S5E and S5F). Rather, low-dose gemcitabine inhibited a specific phenotypic subset revealed by unsupervised clustering on 15 phenotypic and functional Treg markers, primarily defined by expression of *Helios* and *CD103* (Figures 4L and S5G). Prior studies showed that Helios^{+}CD103^{+}GITR^{+} TI-Tregs are the most potently suppressive Treg subset in tumors.[46] With respect to compositional effects of gemcitabine on other immune populations, we noted a putative transient recruitment of polymorphonuclear cells (PMNs) from spleen to tumor (Figure S5H), transient reduction in tumor-infiltrating natural killer (NK) cells at maximum dose (Figure S5I), and induced differentiation of monocytes to macrophages in the tumor (Figures S5J–S5N). Notably, none of these populations exhibited differential effects from low-dose gemcitabine, as was observed for TI-Tregs in this system.

To test whether gemcitabine-mediated myeloid modulation, as observed in our flow cytometry data, may confer a therapeutic benefit independent of Tregs, we compared the effects of low- vs. high-dose gemcitabine on MC38 growth in *Rag1*$^{-/-}$ vs. NSG and C57BL/6J mouse strains. We found identical MC38 growth kinetics in *Rag1*$^{-/-}$ vs. NSG mice, supporting the notion that the effects of low-dose gemcitabine are largely T cell mediated, in line with a prior report (Figure 4M).[45] Taken together, these data suggest that the ability of low-dose gemcitabine to augment responses to immunotherapy in this preclinical model correlate broadly with its effect on TI-Tregs.

Low-dose gemcitabine targets the TI-Treg MR signature

To delineate the mechanism by which low-dose gemcitabine modulates TI-Treg frequency and acquisition of the TI-Treg transcriptional phenotype, we generated scRNA-seq profiles from MC38 tumor- and spleen-derived Tregs, at 24 h after treatment with a single 12 mg/kg dose of either gemcitabine or vehicle control (Figure 5A). For this study, we implanted *FoxP3*$^{Yfp\text{-}Cre}$ mice with MC38 tumor cells to facilitate specific flow-sorting of CD4^{+}FoxP3^{+} Tregs from tumor and spleen using YFP as a FoxP3 expression marker. Using five mice per group, we obtained high-quality profiles from ~10,000 spleen-derived and ~1,000 tumor-derived Tregs from each group (Figure S6A). While raw gene expression data were noisy (Figure S6B), protein activity-based cluster analysis stratified the cells into five clusters (TRC_1–TRC_5) (Figures 5B and S6C), with cluster TRC_3 highly enriched for human TI-Treg MRs, including TRPS1 (Figures 5C and 5D). Notably, this cluster also had highest expression of IKZF2 (Helios), concordant with the gemcitabine-sensitive population of Tregs observed by flow cytometry (Figure 5E). In vehicle-treated control animals, the TRC_3 cluster comprised 7.8% of splenic Tregs vs. 30.1% of TI-Tregs ($p = 1.8 \times 10^{-84}$). Gemcitabine treatment reduced TRC_3 frequency by ~50%, to 14.9% of the TI-Treg cells, while inducing virtually no change in the spleen population (Figures 5F and 5G). Furthermore, treatment resulted in a proportional increase in TRC_1 occupancy, which exhibits signs of interferon exposure (high IFI16 activity). These data suggest that low-dose gemcitabine has antagonistic effects on TI-Tregs and prevents TI-Treg MR activity *in vivo*.

DISCUSSION

Treg immunosuppression in the TME is a major barrier to anti-tumor immunity and undermines the efficacy of checkpoint blockade immunotherapy, which is effective in only a minority of cancer patients.[2,47] To address the critical need for more effective agents to counteract human TI-Treg number or function, we harnessed new tools to identify and validate previously unappreciated regulators of TI- vs. P-Treg transcriptional state. Protein activity analysis—using the VIPER algorithm on a novel dataset of TI-Tregs, P-Tregs, and additional CD4^{+} and CD8^{+} non-Treg controls across 36 patients—identified a set of TI-Treg MRs functionally validated by a pooled *in vivo* CRISPR screen. Most significant among the validated targets was *TRPS1*, a transcription factor not previously studied in the context of Treg biology. In parallel, we conducted a systematic *ex vivo* drug screen and found that gemcitabine possesses preferential cytotoxic capacity against TI-Tregs and inhibits transcriptional activity of TI-Treg MRs, including *TRPS1*, across multiple tumor types. *In vivo* validation studies confirmed that subclinical doses of gemcitabine, lacking activity in immune-deficient animals, effectively potentiated immune-checkpoint blockade-mediated control of established, anti-PD-1-resistant MC38 tumors. These findings have implications for both basic understanding of TI-Treg biology and clinical use of available chemotherapeutics for the purpose of modulating TI-Treg activity. Critically, they provide a highly generalizable integrative framework, both computational and experimental, to identify critical, pharmacologically actionable dependencies of other tolerogenic subpopulations in the TME.

While our findings showing the immune-modulating properties of gemcitabine are broadly consistent with prior reports, they provide critical mechanism-based insight into these effects by elucidating TI-Treg-specific activity of previously unreported MR proteins, especially *TRPS1*, whose activity is inhibited by gemcitabine. While in agreement with prior observations that gemcitabine

Figure 5. Single-cell RNA-sequencing suggests low-dose gemcitabine depletes TI-Tregs exhibiting high TI-Treg master-regulator activity

(A) Schematic of experimental workflow.

(B) Uniform Manifold Approximation and Projection (UMAP) plot and unsupervised clustering by VIPER-inferred protein activity of Tregs from untreated and gemcitabine-treated tumor and spleen. Unique clusters are labelled from 0 - 4, with cluster number and corresponding color conserved in all subsequent figures.

(C) Heatmap of cell-by-cell protein activity for each tumor-Treg MR identified by scRNA-seq, grouped by cluster.

(D) Distribution of the 17-gene TI-Treg MR signature normalized enrichment score by GSEA, grouped by cluster, such that cluster TRC_3 is most enriched for the TI-Treg MR signature.

(E) Distribution of *IKZF2* (Helios) normalized gene expression, grouped by cluster, such that the cluster TRC_3 has highest expression.

(F) Bar plot of cluster frequencies in each sample, such that cluster TRC_3 has a baseline frequency of 7.8% in the spleen of the vehicle control sample and 30.1% in tumor ($p = 1.78 \times 10^{-84}$), with frequency of only 14.9% in tumor of the gemcitabine-treated sample ($p = 1.51 \times 10^{-20}$).

(G) Cox proportional hazard ratios of cluster TRC_3 frequencies in vehicle- vs. gemcitabine-treated mice in tumor (OR = 0.407 [95% CI 0.334–0.494]) and spleen ($p = 0.242$, OR = 1.063 [95% CI 0.958–1.17]).

See also Figure S6.

antagonizes Tregs in mouse and human, our findings also clarify that, at low doses, gemcitabine is differentially toxic in TI- vs. P-Tregs, which was not fully investigated in prior studies.

Specifically, early studies showed that clinically equivalent doses of gemcitabine systemically decrease myeloid-derived suppressor cell (MDSC) and B cell numbers without substantial effects on T cells and, in fact, promote T cell trafficking into tumors.[48–50] In multiple preclinical models, tumor growth in T cell-deficient nude mice or specific $CD8^+$ T cell depletion rendered gemcitabine less effective, suggesting that gemcitabine exhibits T cell-dependent immunogenic activity in addition to direct tumoricidal killing.[45] Informed by prior investigation into the immunogenic effects of low dose or metronomic dosing of other chemotherapeutic agents, such as cyclophosphamide[51–53] or oxaliplatin,[54] more recent studies have shown that subclinical "low" doses of gemcitabine are immunomodulatory in various ways, with effects on NK cell function,[55] myeloid polarization,[56,57] and Tregs.[58–62] However, the mechanisms and effector proteins underlying manifestation of these immunomodulatory effects were not previously identified.

Additional studies are required to more fully understand how gemcitabine selectively modulates TI-Treg MRs. Furthermore, our gemcitabine titration studies in immunocompetent C57BL/6 vs. severely immunodeficient NSG mice defined a more narrow "low dose" range at which gemcitabine is primarily immunomodulatory, building upon previous studies in nude mice that were confounded by the presence of functional NK and myeloid cells, as these are also known to be modulated by gemcitabine.[45,55] Our flow cytometry profiling and therapeutic studies further inform these prior observations and confirm a T cell-mediated immunomodulatory effect by showing lack of response to low-dose gemcitabine in $RAG1^{-/-}$ mice. We found the range between 3 and 10 mg/kg of gemcitabine dosed every 3 days to be immunogenic, which represents 2.5%–8.3% of the standard murine maximum tolerated dose of 120 mg/kg and roughly translates to a human equivalent dose[63] of 9–30 mg/m^2, compared with the standard clinical dose of 1,000 mg/m^2. Although we fully acknowledge the challenges of translating dosing strategies between species, our studies support the development of dose-finding studies of gemcitabine in combination with immune-modulating agents such as anti-PD-1, particularly in settings where the benefit of anti-PD-1 monotherapy is suboptimal or in long-term maintenance therapy.

A major finding of our study was the discovery and validation of *TRPS1* as a putative MR of TI-Tregs, such that CRISPR KO targeting of *Trps1* inhibits tumor Treg infiltration without depleting P-Tregs, preferentially inhibits TI-Tregs relative to tumor $CD4^+$ Tconv, and inhibits overall tumor growth, with a 54% cure rate in the MCA205 tumor model without exogenous intervention. Conversely, overexpression of *TRPS1* induces the entire module of TI-Treg MRs and drives P-Tregs toward a TI-Treg transcriptional phenotype. *TRPS1* is a transcription factor classically linked to skeletal development, as subjects with germline alterations in the *Trps1* gene suffer from autosomal dominant trichorhinophalangeal syndromes with characteristic craniofacial abnormalities.[64,65] More recently, *TRPS1* has been implicated in tumorigenesis in breast cancer[66,67] and osteosarcoma,[68] potentially through promotion of dysregulated cell replication resulting in accumulation of genomic aberrations.[69] Functionally, *TRPS1* is thought to function uniquely as a transcriptional repressor via its GATA domain,[70] although, notably, *TRPS1* contains two Ikaros-like domains, whose specific functions are poorly characterized. Other Ikaros family proteins, including Helios and Aiolos, are expressed in hematopoietic tissues with important functions in Treg differentiation and function[46,71,72]; thus, it is tempting to speculate that *TRPS1* governs TI-Treg activities via its Ikaros domain. At this point, the specific functions of *TRPS1* in Tregs remain to be described and additional future work is warranted to understand the mechanisms of *TRPS1* regulation in Tregs both within and outside of the TME. In addition, our results support the design of specific inhibitors of *TRPS1* activity. Compared with Treg-targeting agents in clinical translation, such as CCR8, which is relatively TI-Treg-specific but not required for Treg function,[16,19] TRPS1 as a putative target has the benefit of being TI-Treg specific, functionally required for TI-Treg recruitment and/or retention, present in TI-Tregs across multiple cancer types, and, in certain cases, also present in malignant cells.[66–68]

Together, the integrative systems biology approach proposed here—combining CRISPR validation of putative regulatory proteins in an *in vivo* functional genomics system with *ex vivo* drug screening and transcriptional profiling of treatment response—provides a highly generalizable framework for the systematic discovery of Treg-directed immunotherapy targets. Of note, this platform could in theory be extended to other tolerogenic cell types in the TME, opening up additional possibilities for target identification and validation across the field of immune oncology. Furthermore, our PLATE-seq screening method can be feasibly extended to significantly larger compound libraries, thus supporting the discovery of additional TI-Treg modulating compounds. While the development of TRPS1-directed therapeutics will require additional effort, our findings on low-dose gemcitabine are readily translatable to human studies aimed at improving the clinical activity of anti-PD(L)-1 agents in the clinic.

Limitations of the study

Future follow-up studies may further clarify the mechanism of *TRPS1* function in TI-Tregs *in vivo* by generating Treg-lineage-specific *TRPS1* KO mice and performing further scRNA-seq and immunophenotyping in these mice across tissue contexts. The loss of *TRPS1* across all immune lineages in our present model represents a limitation of the study such that a potential contribution of *TRPS1* KO in other immune cell types to improved overall survival cannot entirely be ruled out. Relatedly, evidence for Tregs mediating response to low-dose gemcitabine in this study is correlative based on observed depletion of intratumoral Tregs by flow cytometry and of the TI-Treg transcriptional subphenotype in particular by scRNA-seq. We cannot fully rule out a contribution of effects on other immune cell subtypes, downstream of or in parallel to the observed effect on TI-Tregs, as contributing to overall treatment response. Finally, differences in the engraftment rate of sgRNA-bearing stem cells in our chimeric mouse model result in lower statistical power for certain proteins in the pooled screen. As a result, while we have functionally validated eight of the predicted TI-Treg MRs, including *TRPS1*, further repeat cohorts may validate additional predicted MRs that had a lower baseline engraftment rate in our study.

STAR★METHODS

Detailed methods are provided in the online version of this paper and include the following:

- KEY RESOURCES TABLE
- RESOURCE AVAILABILITY
  - Lead contact
  - Materials availability
  - Data and code availability
- EXPERIMENTAL MODEL AND SUBJECT DETAILS
  - Cell lines
  - Primary cell cultures
  - Animals
- METHOD DETAILS
  - Clinical sample collection, sorting, and RNA-sequencing
  - Gene expression and VIPER analysis
  - Random Forest Feature Selection
  - CRISPR KO library design
  - CRISPR KO oligo synthesis and library cloning
  - Lentiviral packaging of the sgRNA library
  - sgRNA library transductions into hematopoietic LSK cells
  - CRISPR validation in chimeric immune editing model
  - Genomic DNA extraction and preparation of NGS libraries
  - *In vivo* CRISPR KO-screen analysis
  - CRISPR KO-based tumor growth experiments
  - ORF cloning for transcription factor overexpression/reprogramming assay
  - Transcription factor overexpression / reprogramming assay (scRNA-Seq)
  - High-throughput Treg-directed drug screening
  - Drug-based tumor growth experiments
  - *In vitro* Treg suppression assay
  - Histology
  - High dimensional spectral flow cytometry immune profiling
  - Single-cell RNA-seq profiling of gemcitabine effect on TI-Tregs
- QUANTIFICATION AND STATISTICAL ANALYSIS

SUPPLEMENTAL INFORMATION

Supplemental information can be found online at https://doi.org/10.1016/j.ccell.2023.04.003.

ACKNOWLEDGMENTS

This research was supported by National Institutes of Health (NIH) grants R01 CA127153, 1P50CA58236-15, and P30CA006973, the Prostate Cancer Foundation Challenge Grant, and CUMC institutional funds to C.G.D.; by NIH grants R35CA197745, U01CA272610, S10 OD012351, and S10 OD021764 to A.C.; by NIH grant F30CA260765-01 to A.O.; and by NIH grants UL1TR001873 and TL1TR001875 to C.A. This study was also supported by the Sigrid Jusélius Foundation (M.T.). We thank the Sidney Kimmel Comprehensive Cancer Center Experimental and Computational Genomics Core at Johns Hopkins, supported by NIH/NCI grant P30CA006973, for support in performing the bulk-RNA sequencing on sorted cells from human cancer subjects. We also thank Drs. A. Jolma and J. Taipale for kindly providing some of the full-length cDNA of the TI-TREG MRs. This study was also supported by the NIH/NCI SPORE in Prostate Cancer (P50CA58236) and the US Department of Defense Prostate Cancer Research Program (PCRP) Prostate Cancer Biospecimen Network Site (W81XWH-18-2-0015).

AUTHOR CONTRIBUTIONS

A.O. conceived of, coordinated, and assisted in performing experiments; performed data analysis; and co-wrote the manuscript. C.A. conceived of, designed, and performed all experiments; designed all flow cytometry panels; and co-wrote the manuscript. M.T. conceived of and aided in design of experiments and optimized and performed all CRISPR-based protocols. M.K.-M. assisted in hematopoietic stem cell transplantation. C.M.J., T.N., C.M.K., M.A., T.B., A.M.D., and M.L. recruited patients and coordinated collection of tumor and peripheral blood specimens for sorted T cell bulk RNA-seq. C.K. ran the high-throughput drug screen PLATE-seq assay. A.C. and C.G.D. conceived of the project, advised on overall experimental design and data analysis procedure, and co-wrote the manuscript.

DECLARATION OF INTERESTS

C.G.D. is a co-inventor on patents licensed from JHU to BMS and Janssen; has served as a paid consultant to AZ Medimmune, BMS, Pfizer, Roche, Sanofi Aventis, Genentech, Merck, and Janssen; and has received sponsored research funding to his institution from BMS lioN and Janssen. A.C. is founder, equity holder, consultant, and director of DarwinHealth, Inc., which has licensed IP related to these algorithms from Columbia University. Columbia University is an equity holder in DarwinHealth, Inc. S.Y. has received sponsored research support to his institution from Celgene/BMS, Janssen, and Cepheid/Danaher and has served as a paid consultant to Cepheid/Danaher. A.O., C.A., C.G.D., and A.C. are co-inventors on US provisional patent no. 63/188,970, "Therapeutic modulation of regulatory T cells through master regulatory protein targeting," which relates to the work described here.

Received: April 1, 2022
Revised: September 13, 2022
Accepted: April 6, 2023
Published: April 27, 2023

REFERENCES

1. Schreiber, R.D., Old, L.J., and Smyth, M.J. (2011). Cancer immunoediting: integrating immunity's roles in cancer suppression and promotion. Science *331*, 1565–1570.
2. Chao, J.L., and Savage, P.A. (2018). Unlocking the complexities of tumor-associated regulatory T cells. J. Immunol. *200*, 415–421.
3. Flammiger, A., Weisbach, L., Huland, H., Tennstedt, P., Simon, R., Minner, S., Bokemeyer, C., Sauter, G., Schlomm, T., and Trepel, M. (2013). High tissue density of FOXP3+ T cells is associated with clinical outcome in prostate cancer. Eur. J. Cancer *49*, 1273–1279.
4. Muroyama, Y., Nirschl, T.R., Kochel, C.M., Lopez-Bujanda, Z., Theodros, D., Mao, W., Carrera-Haro, M.A., Ghasemzadeh, A., Marciscano, A.E., Velarde, E., et al. (2017). Stereotactic radiotherapy increases functionally suppressive regulatory T cells in the tumor microenvironment. Cancer Immunol. Res. *5*, 992–1004.
5. Obradovic, A.Z., Dallos, M.C., Zahurak, M.L., Partin, A.W., Schaeffer, E.M., Ross, A.E., Allaf, M.E., Nirschl, T.R., Liu, D., Chapman, C.G., et al. (2020). T-cell infiltration and adaptive Treg resistance in response to androgen deprivation with or without vaccination in localized prostate cancer. Clin. Cancer Res. *26*, 3182–3192.
6. Shang, B., Liu, Y., Jiang, S.-j., and Liu, Y. (2015). Prognostic value of tumor-infiltrating FoxP3+ regulatory T cells in cancers: a systematic review and meta-analysis. Sci. Rep. *5*, 15179.
7. Bos, P.D., Plitas, G., Rudra, D., Lee, S.Y., and Rudensky, A.Y. (2013). Transient regulatory T cell ablation deters oncogene-driven breast cancer and enhances radiotherapy. J. Exp. Med. *210*, 2435–2466.

8. Freeman, Z.T., Nirschl, T.R., Hovelson, D.H., Johnston, R.J., Engelhardt, J.J., Selby, M.J., Kochel, C.M., Lan, R.Y., Zhai, J., Ghasemzadeh, A., et al. (2020). A conserved intratumoral regulatory T cell signature identifies 4-1BB as a pan-cancer target. J. Clin. Invest. *130*, 1405–1416.
9. Selby, M.J., Engelhardt, J.J., Quigley, M., Henning, K.A., Chen, T., Srinivasan, M., and Korman, A.J. (2013). Anti-CTLA-4 antibodies of IgG2a isotype enhance antitumor activity through reduction of intratumoral regulatory T cells. Cancer Immunol. Res. *1*, 32–42.
10. Sharma, A., Subudhi, S.K., Blando, J., Scutti, J., Vence, L., Wargo, J., Allison, J.P., Ribas, A., and Sharma, P. (2019). Anti-CTLA-4 immunotherapy does not deplete FOXP3(+) regulatory T cells (Tregs) in human cancers. Clin. Cancer Res. *25*, 1233–1238.
11. Simpson, T.R., Li, F., Montalvo-Ortiz, W., Sepulveda, M.A., Bergerhoff, K., Arce, F., Roddie, C., Henry, J.Y., Yagita, H., Wolchok, J.D., et al. (2013). Fc-dependent depletion of tumor-infiltrating regulatory T cells co-defines the efficacy of anti-CTLA-4 therapy against melanoma. J. Exp. Med. *210*, 1695–1710.
12. De Simone, M., Arrigoni, A., Rossetti, G., Gruarin, P., Ranzani, V., Politano, C., Bonnal, R.J.P., Provasi, E., Sarnicola, M.L., Panzeri, I., et al. (2016). Transcriptional landscape of human tissue lymphocytes unveils uniqueness of tumor-infiltrating T regulatory cells. Immunity *45*, 1135–1147.
13. Magnuson, A.M., Kiner, E., Ergun, A., Park, J.S., Asinovski, N., Ortiz-Lopez, A., Kilcoyne, A., Paoluzzi-Tomada, E., Weissleder, R., Mathis, D., et al. (2018). Identification and validation of a tumor-infiltrating Treg transcriptional signature conserved across species and tumor types. Proc. Natl. Acad. Sci. USA *115*, E10672–E10681.
14. Plitas, G., Konopacki, C., Wu, K., Bos, P.D., Morrow, M., Putintseva, E.V., Chudakov, D.M., and Rudensky, A.Y. (2016). Regulatory T cells exhibit distinct features in human breast cancer. Immunity *45*, 1122–1134.
15. Zheng, C., Zheng, L., Yoo, J.-K., Guo, H., Zhang, Y., Guo, X., Kang, B., Hu, R., Huang, J.Y., Zhang, Q., et al. (2017). Landscape of infiltrating T cells in liver cancer revealed by single-cell sequencing. Cell *169*, 1342–1356.e16.
16. Van Damme, H., Dombrecht, B., Kiss, M., Roose, H., Allen, E., Van Overmeire, E., Kancheva, D., Martens, L., Murgaski, A., Bardet, P.M.R., et al. (2021). Therapeutic depletion of CCR8(+) tumor-infiltrating regulatory T cells elicits antitumor immunity and synergizes with anti-PD-1 therapy. J. Immunother. Cancer *9*, e001749.
17. Andrews, L.P., Marciscano, A.E., Drake, C.G., and Vignali, D.A.A. (2017). LAG3 (CD223) as a cancer immunotherapy target. Immunol. Rev. *276*, 80–96.
18. Tawbi, H.A., Schadendorf, D., Lipson, E.J., Ascierto, P.A., Matamala, L., Castillo Gutiérrez, E., Rutkowski, P., Gogas, H.J., Lao, C.D., De Menezes, J.J., et al. (2022). Relatlimab and nivolumab versus nivolumab in untreated advanced melanoma. N. Engl. J. Med. *386*, 24–34.
19. Whiteside, S.K., Grant, F.M., Gyori, D.S., Conti, A.G., Imianowski, C.J., Kuo, P., Nasrallah, R., Sadiyah, F., Lira, S.A., Tacke, F., et al. (2021). CCR8 marks highly suppressive Treg cells within tumours but is dispensable for their accumulation and suppressive function. Immunology *163*, 512–520.
20. Basso, K., Margolin, A.A., Stolovitzky, G., Klein, U., Dalla-Favera, R., and Califano, A. (2005). Reverse engineering of regulatory networks in human B cells. Nat. Genet. *37*, 382–390.
21. Alvarez, M.J., Shen, Y., Giorgi, F.M., Lachmann, A., Ding, B.B., Ye, B.H., and Califano, A. (2016). Functional characterization of somatic mutations in cancer using network-based inference of protein activity. Nat. Genet. *48*, 838–847.
22. Aytes, A., Mitrofanova, A., Lefebvre, C., Alvarez, M.J., Castillo-Martin, M., Zheng, T., Eastham, J.A., Gopalan, A., Pienta, K.J., Shen, M.M., et al. (2014). Cross-species regulatory network analysis identifies a synergistic interaction between FOXM1 and CENPF that drives prostate cancer malignancy. Cancer Cell *25*, 638–651.
23. Carro, M.S., Lim, W.K., Alvarez, M.J., Bollo, R.J., Zhao, X., Snyder, E.Y., Sulman, E.P., Anne, S.L., Doetsch, F., Colman, H., et al. (2010). The transcriptional network for mesenchymal transformation of brain tumours. Nature *463*, 318–325.
24. Paull, E.O., Aytes, A., Jones, S.J., Subramaniam, P.S., Giorgi, F.M., Douglass, E.F., Tagore, S., Chu, B., Vasciaveo, A., Zheng, S., et al. (2021). A modular master regulator landscape controls cancer transcriptional identity. Cell *184*, 334–351.e20.
25. Obradovic, A., Chowdhury, N., Haake, S.M., Ager, C., Wang, V., Vlahos, L., Guo, X.V., Aggen, D.H., Rathmell, W.K., Jonasch, E., et al. (2021). Single-cell protein activity analysis identifies recurrence-associated renal tumor macrophages. Cell *184*, 2988–3005.e16.
26. Son, J., Ding, H., Farb, T.B., Efanov, A.M., Sun, J., Gore, J.L., Syed, S.K., Lei, Z., Wang, Q., Accili, D., et al. (2021). BACH2 inhibition reverses β cell failure in type 2 diabetes models. J. Clin. Invest. *131*, e153876.
27. Califano, A., and Alvarez, M.J. (2017). The recurrent architecture of tumour initiation, progression and drug sensitivity. Nat. Rev. Cancer *17*, 116–130.
28. Elyada, E., Bolisetty, M., Laise, P., Flynn, W.F., Courtois, E.T., Burkhart, R.A., Teinor, J.A., Belleau, P., Biffi, G., Lucito, M.S., et al. (2019). Cross-species single-cell analysis of pancreatic ductal adenocarcinoma reveals antigen-presenting cancer-associated fibroblasts. Cancer Discov. *9*, 1102–1123.
29. Obradovic, A., Graves, D., Korrer, M., Wang, Y., Roy, S., Naveed, A., Xu, Y., Luginbuhl, A., Curry, J., Gibson, M., et al. (2022). Immunostimulatory cancer-associated fibroblast subpopulations can predict immunotherapy response in head and neck cancer. Clin. Cancer Res. *28*, 2094–2109.
30. LaFleur, M.W., Nguyen, T.H., Coxe, M.A., Yates, K.B., Trombley, J.D., Weiss, S.A., Brown, F.D., Gillis, J.E., Coxe, D.J., Doench, J.G., et al. (2019). A CRISPR-Cas9 delivery system for in vivo screening of genes in the immune system. Nat. Commun. *10*, 1668.
31. Alvarez, M.J., Subramaniam, P.S., Tang, L.H., Grunn, A., Aburi, M., Rieckhof, G., Komissarova, E.V., Hagan, E.A., Bodei, L., Clemons, P.A., et al. (2018). A precision oncology approach to the pharmacological targeting of mechanistic dependencies in neuroendocrine tumors. Nat. Genet. *50*, 979–989.
32. Lachmann, A., Giorgi, F.M., Lopez, G., and Califano, A. (2016). ARACNe-AP: gene network reverse engineering through adaptive partitioning inference of mutual information. Bioinformatics *32*, 2233–2235.
33. Subramanian, A., Tamayo, P., Mootha, V.K., Mukherjee, S., Ebert, B.L., Gillette, M.A., Paulovich, A., Pomeroy, S.L., Golub, T.R., Lander, E.S., et al. (2005). Gene set enrichment analysis: a knowledge-based approach for interpreting genome-wide expression profiles. Proc. Natl. Acad. Sci. USA *102*, 15545–15550.
34. Bandukwala, H.S., and Rao, A. (2013). 'Nurr'ishing Treg cells: Nr4a transcription factors control Foxp3 expression. Nat. Immunol. *14*, 201–203.
35. Renoux, F., Stellato, M., Haftmann, C., Vogetseder, A., Huang, R., Subramaniam, A., Becker, M.O., Blyszczuk, P., Becher, B., Distler, J.H.W., et al. (2020). The AP1 transcription factor Fosl2 promotes systemic autoimmunity and inflammation by repressing Treg development. Cell Rep. *31*, 107826.
36. Rocamora-Reverte, L., Tuzlak, S., von Raffay, L., Tisch, M., Fiegl, H., Drach, M., Reichardt, H.M., Villunger, A., Tischner, D., and Wiegers, G.J. (2019). Glucocorticoid receptor-deficient Foxp3(+) regulatory T cells fail to control experimental inflammatory Bowel disease. Front. Immunol. *10*, 472.
37. Morita, K., Okamura, T., Inoue, M., Komai, T., Teruya, S., Iwasaki, Y., Sumitomo, S., Shoda, H., Yamamoto, K., and Fujio, K. (2016). Egr2 and Egr3 in regulatory T cells cooperatively control systemic autoimmunity through Ltbp3-mediated TGF-β3 production. Proc. Natl. Acad. Sci. USA *113*, E8131–E8140.
38. Arce Vargas, F., Furness, A.J.S., Litchfield, K., Joshi, K., Rosenthal, R., Ghorani, E., Solomon, I., Lesko, M.H., Ruef, N., Roddie, C., et al. (2018). Fc effector function contributes to the activity of human anti-CTLA-4 antibodies. Cancer Cell *33*, 649–663.e4.

39. Pfirschke, C., Engblom, C., Rickelt, S., Cortez-Retamozo, V., Garris, C., Pucci, F., Yamazaki, T., Poirier-Colame, V., Newton, A., Redouane, Y., et al. (2016). Immunogenic chemotherapy sensitizes tumors to checkpoint blockade therapy. Immunity *44*, 343–354.

40. Bush, E.C., Ray, F., Alvarez, M.J., Realubit, R., Li, H., Karan, C., Califano, A., and Sims, P.A. (2017). PLATE-Seq for genome-wide regulatory network analysis of high-throughput screens. Nat. Commun. *8*, 105.

41. Douglass, E.F., Allaway, R.J., Szalai, B., Wang, W., Tian, T., Fernández-Torras, A., Realubit, R., Karan, C., Zheng, S., Pessia, A., et al. (2020). A Community Challenge for Pancancer Drug Mechanism of Action Inference from Perturbational Profile Data (Cold Spring Harbor Laboratory).

42. Taylor, M.A., Hughes, A.M., Walton, J., Coenen-Stass, A.M.L., Magiera, L., Mooney, L., Bell, S., Staniszewska, A.D., Sandin, L.C., Barry, S.T., et al. (2019). Longitudinal immune characterization of syngeneic tumor models to enable model selection for immune oncology drug discovery. J. Immunother. Cancer *7*, 328.

43. Ager, C.R., Boda, A., Rajapakshe, K., Lea, S.T., Di Francesco, M.E., Jayaprakash, P., Slay, R.B., Morrow, B., Prasad, R., Dean, M.A., et al. (2021). High potency STING agonists engage unique myeloid pathways to reverse pancreatic cancer immune privilege. J. Immunother. Cancer *9*, e003246.

44. Beatty, G.L., Chiorean, E.G., Fishman, M.P., Saboury, B., Teitelbaum, U.R., Sun, W., Huhn, R.D., Song, W., Li, D., Sharp, L.L., et al. (2011). CD40 agonists alter tumor stroma and show efficacy against pancreatic carcinoma in mice and humans. Science *331*, 1612–1616.

45. Suzuki, E., Sun, J., Kapoor, V., Jassar, A.S., and Albelda, S.M. (2007). Gemcitabine has significant immunomodulatory activity in murine tumor models independent of its cytotoxic effects. Cancer Biol. Ther. *6*, 880–885.

46. Zabransky, D.J., Nirschl, C.J., Durham, N.M., Park, B.V., Ceccato, C.M., Bruno, T.C., Tam, A.J., Getnet, D., and Drake, C.G. (2012). Phenotypic and functional properties of Helios+ regulatory T cells. PLoS One *7*, e34547.

47. Zappasodi, R., Merghoub, T., and Wolchok, J.D. (2018). Emerging concepts for immune checkpoint blockade-based combination therapies. Cancer Cell *33*, 581–598.

48. Daikeler, T., Maas, K., Weiss, B., Hartmann, J., Knobloch, A., Arning, M., Kanz, L., and Bokemeyer, C. (1997). The influence of gemcitabine on the CD4/CD8 ratio in patients with solid tumours. Oncol. Rep. *4*, 561–564.

49. Nowak, A.K., Robinson, B.W.S., and Lake, R.A. (2002). Gemcitabine exerts a selective effect on the humoral immune response: implications for combination chemo-immunotherapy. Cancer Res. *62*, 2353–2358.

50. Suzuki, E., Kapoor, V., Jassar, A.S., Kaiser, L.R., and Albelda, S.M. (2005). Gemcitabine selectively eliminates splenic Gr-1+/CD11b+ myeloid suppressor cells in tumor-bearing animals and enhances antitumor immune activity. Clin. Cancer Res. *11*, 6713–6721.

51. Ghiringhelli, F., Menard, C., Puig, P.E., Ladoire, S., Roux, S., Martin, F., Solary, E., Le Cesne, A., Zitvogel, L., and Chauffert, B. (2007). Metronomic cyclophosphamide regimen selectively depletes CD4+CD25+ regulatory T cells and restores T and NK effector functions in end stage cancer patients. Cancer Immunol. Immunother. *56*, 641–648.

52. Lutsiak, M.E.C., Semnani, R.T., De Pascalis, R., Kashmiri, S.V.S., Schlom, J., and Sabzevari, H. (2005). Inhibition of CD4+25+ T regulatory cell function implicated in enhanced immune response by low-dose cyclophosphamide. Blood *105*, 2862–2868.

53. Wada, S., Yoshimura, K., Hipkiss, E.L., Harris, T.J., Yen, H.-R., Goldberg, M.V., Grosso, J.F., Getnet, D., Demarzo, A.M., Netto, G.J., et al. (2009). Cyclophosphamide augments antitumor immunity: studies in an autochthonous prostate cancer model. Cancer Res. *69*, 4309–4318.

54. Shalapour, S., Font-Burgada, J., Di Caro, G., Zhong, Z., Sanchez-Lopez, E., Dhar, D., Willimsky, G., Ammirante, M., Strasner, A., Hansel, D.E., et al. (2015). Immunosuppressive plasma cells impede T-cell-dependent immunogenic chemotherapy. Nature *521*, 94–98.

55. Zhang, X., Wang, D., Li, Z., Jiao, D., Jin, L., Cong, J., Zheng, X., and Xu, L. (2020). Low-dose gemcitabine treatment enhances immunogenicity and natural killer cell-driven tumor immunity in lung cancer. Front. Immunol. *11*, 331.

56. Deshmukh, S.K., Tyagi, N., Khan, M.A., Srivastava, S.K., Al-Ghadhban, A., Dugger, K., Carter, J.E., Singh, S., and Singh, A.P. (2018). Gemcitabine treatment promotes immunosuppressive microenvironment in pancreatic tumors by supporting the infiltration, growth, and polarization of macrophages. Sci. Rep. *8*, 12000.

57. Di Caro, G., Cortese, N., Castino, G.F., Grizzi, F., Gavazzi, F., Ridolfi, C., Capretti, G., Mineri, R., Todoric, J., Zerbi, A., et al. (2016). Dual prognostic significance of tumour-associated macrophages in human pancreatic adenocarcinoma treated or untreated with chemotherapy. Gut *65*, 1710–1720.

58. Homma, Y., Taniguchi, K., Nakazawa, M., Matsuyama, R., Mori, R., Takeda, K., Ichikawa, Y., Tanaka, K., and Endo, I. (2014). Changes in the immune cell population and cell proliferation in peripheral blood after gemcitabine-based chemotherapy for pancreatic cancer. Clin. Transl. Oncol. *16*, 330–335.

59. Rettig, L., Seidenberg, S., Parvanova, I., Samaras, P., Curioni, A., Knuth, A., and Pascolo, S. (2011). Gemcitabine depletes regulatory T-cells in human and mice and enhances triggering of vaccine-specific cytotoxic T-cells. Int. J. Cancer *129*, 832–838.

60. Shevchenko, I., Karakhanova, S., Soltek, S., Link, J., Bayry, J., Werner, J., Umansky, V., and Bazhin, A.V. (2013). Low-dose gemcitabine depletes regulatory T cells and improves survival in the orthotopic Panc02 model of pancreatic cancer. Int. J. Cancer *133*, 98–107.

61. Skavatsou, E., Semitekolou, M., Morianos, I., Karampelas, T., Lougiakis, N., Xanthou, G., and Tamvakopoulos, C. (2021). Immunotherapy combined with metronomic dosing: an effective approach for the treatment of NSCLC. Cancers *13*, 1901.

62. Tongu, M., Harashima, N., Monma, H., Inao, T., Yamada, T., Kawauchi, H., and Harada, M. (2013). Metronomic chemotherapy with low-dose cyclophosphamide plus gemcitabine can induce anti-tumor T cell immunity in vivo. Cancer Immunol. Immunother. *62*, 383–391.

63. Nair, A.B., and Jacob, S. (2016). A simple practice guide for dose conversion between animals and human. J. Basic Clin. Pharm. *7*, 27–31.

64. Lüdecke, H.J., Schaper, J., Meinecke, P., Momeni, P., Gross, S., von Holtum, D., Hirche, H., Abramowicz, M.J., Albrecht, B., Apacik, C., et al. (2001). Genotypic and phenotypic spectrum in tricho-rhino-phalangeal syndrome types I and III. Am. J. Hum. Genet. *68*, 81–91.

65. Momeni, P., Glöckner, G., Schmidt, O., von Holtum, D., Albrecht, B., Gillessen-Kaesbach, G., Hennekam, R., Meinecke, P., Zabel, B., Rosenthal, A., et al. (2000). Mutations in a new gene, encoding a zinc-finger protein, cause tricho-rhino-phalangeal syndrome type I. Nat. Genet. *24*, 71–74.

66. Ai, D., Yao, J., Yang, F., Huo, L., Chen, H., Lu, W., Soto, L.M.S., Jiang, M., Raso, M.G., Wang, S., et al. (2021). TRPS1: a highly sensitive and specific marker for breast carcinoma, especially for triple-negative breast cancer. Mod. Pathol. *34*, 710–719.

67. Cornelissen, L.M., Drenth, A.P., van der Burg, E., de Bruijn, R., Pritchard, C.E.J., Huijbers, I.J., Zwart, W., and Jonkers, J. (2020). TRPS1 acts as a context-dependent regulator of mammary epithelial cell growth/differentiation and breast cancer development. Genes Dev. *34*, 179–193.

68. Li, Z., Jia, M., Wu, X., Cui, J., Pan, A., and Li, L. (2015). Overexpression of Trps1 contributes to tumor angiogenesis and poor prognosis of human osteosarcoma. Diagn. Pathol. *10*, 167.

69. Yang, J., Liu, X., Huang, Y., He, L., Zhang, W., Ren, J., Wang, Y., Wu, J., Wu, X., Shan, L., et al. (2021). TRPS1 drives heterochromatic origin refiring and cancer genome evolution. Cell Rep. *34*, 108814.

70. Malik, T.H., Von Stechow, D., Bronson, R.T., and Shivdasani, R.A. (2002). Deletion of the GATA domain of TRPS1 causes an absence of facial hair and provides new insights into the bone disorder in inherited tricho-rhino-phalangeal syndromes. Mol. Cell Biol. *22*, 8592–8600.

71. Getnet, D., Grosso, J.F., Goldberg, M.V., Harris, T.J., Yen, H.-R., Bruno, T.C., Durham, N.M., Hipkiss, E.L., Pyle, K.J., Wada, S., et al. (2010). A role for the transcription factor Helios in human CD4(+)CD25(+) regulatory T cells. Mol. Immunol. *47*, 1595–1600.

72. Thornton, A.M., Korty, P.E., Tran, D.Q., Wohlfert, E.A., Murray, P.E., Belkaid, Y., and Shevach, E.M. (2010). Expression of Helios, an Ikaros transcription factor family member, differentiates thymic-derived from peripherally induced Foxp3+ T regulatory cells. J. Immunol. *184*, 3433–3441.

73. Doench, J.G., Fusi, N., Sullender, M., Hegde, M., Vaimberg, E.W., Donovan, K.F., Smith, I., Tothova, Z., Wilen, C., Orchard, R., et al. (2016). Optimized sgRNA design to maximize activity and minimize off-target effects of CRISPR-Cas9. Nat. Biotechnol. *34*, 184–191. https://doi.org/10.1038/nbt.3437.

74. Hockemeyer, D., Soldner, F., Cook, E.G., Gao, Q., Mitalipova, M., and Jaenisch, R. (2008). A drug-inducible system for direct reprogramming of human somatic cells to pluripotency. Cell Stem Cell *3*, 346–353.

75. Hao, Y., Hao, S., Andersen-Nissen, E., Mauck, W.M., 3rd, Zheng, S., Butler, A., Lee, M.J., Wilk, A.J., Darby, C., Zager, M., et al. (2021). Integrated analysis of multimodal single-cell data. Cell *184*, 3573–3587.e29.

STAR★METHODS

KEY RESOURCES TABLE

REAGENT or RESOURCE	SOURCE	IDENTIFIER
Antibodies		
Anti-Mouse TCR-β BUV395 (clone H57-597)	BD	Cat# 742485
Anti-Mouse CD103 BUV496 (clone M290)	BD	Cat# 741083
Anti-Mouse CD44 BUV563 (clone IM7)	BD	Cat# 741227
Anti-Mouse PD-1 BUV615 (clone J43)	BD	Cat# 752299
Anti-Mouse Nrp1 BUV661 (clone V46-1954)	BD	Cat# 752461
Anti-Mouse/Human Ki67 BUV737 (clone B56)	BD	Cat# 567130
Anti-Mouse CD4 BUV805 (clone GK1.5)	BD	Cat# 612900
Anti-Mouse CD39 BV421 (clone Y23-1185)	BD	Cat# 567105
Anti-Mouse IA-IE Pacific Blue (clone M5/114.15.2)	BioLegend	Cat# 107620
Anti-Mouse ST2 BV480 (clone U29-93)	BD	Cat# 746701
Anti-Mouse CD8 Pacific Orange (clone 5H10)	ThermoFisher Scientific	Cat# MCD0830
Anti-Mouse CD62L BV570 (clone MEL-14)	BioLegend	Cat# 104433
Anti-Mouse CD11c BV605 (clone N418)	BioLegend	Cat# 117334
Anti-Mouse ICOS BV650 (clone C398.4A)	BioLegend	Cat# 313550
Anti-Mouse KLRG1 BV750 (clone 2F1)	BD	Cat# 746972
Anti-Mouse PD-L1 BV785 (clone MIH5)	BD	Cat# 741014
Anti-Mouse iNOS FITC (clone REA982)	Miltenyi Biotec	Cat# 130-116-357
Anti-Mouse CD45 A532 (clone 30-F11)	ThermoFisher Scientific	Cat# 58-0451-82
Anti-Mouse CD19 NB610 (clone 1D3)	ThermoFisher Scientific	Cat# M004T02B06
Anti-Mouse Ly6C PerCP-Cy5.5 (clone HK1.4)	BioLegend	Cat# 128012
Anti-Mouse CD206 PerCPeF710 (clone MR6F3)	ThermoFisher Scientific	Cat# 46-2069-42
Anti-Mouse/Human TOX PE (clone REA473)	Miltenyi Biotec	Cat# 130-120-716
Anti-Mouse Ly6G SYG563 (clone 1A8)	BioLegend	Cat# 127668
Anti-Mouse Helios PE-Dazzle 594 (clone 22F6)	BioLegend	Cat# 137232
Anti-Mouse CD80 PE-Cy5 (clone 16-10A1)	BioLegend	Cat# 104712
Anti-Mouse FoxP3 PE-Cy7 (clone FJK-16s)	ThermoFisher Scientific	Cat# 25-5773-82
Anti-Mouse/Human B220 PE/Fire 810 (clone RA3-6B2)	BioLegend	Cat# 103287
Anti-Mouse/Human TCF-1 APC (clone C63D9)	Cell Signaling Technologies	Cat# 37636S
Anti-Mouse CD69 SNIR685 (clone H1.2F3)	BioLegend	Cat# 104558
Anti-Mouse/Human CD11b A700 (clone M1/70)	BioLegend	Cat# 101222
Anti-Mouse F4/80 APC/Fire 750 (clone BM8)	BioLegend	Cat# 123152
Anti-Mouse NK1.1 APC/Fire 810 (clone S17016D)	BioLegend	Cat# 156519
TruStain FcX PLUS (clone S17011E)	BioLegend	Cat# 156604
Anti-Mouse Ter-119 PE (clone TER-119)	BioLegend	Cat# 116208
Anti-Mouse/Human CD11b PE (clone M1/70)	BioLegend	Cat# 101208
Anti-Mouse Gr-1 PE (clone RBC-8C5)	BioLegend	Cat# 108408
Anti-Mouse CD3ε PE (clone 145-2C11)	BioLegend	Cat# 100308
Anti-Mouse CD5 PE (clone 53-7.3)	BioLegend	Cat# 100608
Anti-Mouse/Human B220 PE (clone RA3-6B2)	BioLegend	Cat# 103208
Anti-Mouse CD117 (c-kit) APC (clone 2B8)	BioLegend	Cat# 105812
Anti-Mouse Sca-1 BV421 (clone D7)	BioLegend	Cat# 108127
Anti-Human CD4 BV421 (clone OKT-4)	BioLegend	Cat# 317434
Anti-Human CD25 APC (clone M-A251)	BioLegend	Cat# 356110

(*Continued on next page*)

Continued

REAGENT or RESOURCE	SOURCE	IDENTIFIER
Anti-Human CD127 PE (clone A019D5)	BioLegend	Cat# 351304
Anti-Mouse CD25 BV421 (clone PC61)	BioLegend	Cat# 102043
Anti-Mouse CD3 BV711 (clone 145-2C11)	BioLegend	Cat# 100349
Anti-Mouse CD8 PE (clone 53-6.7)	BioLegend	Cat# 100708
Anti-Mouse CD127 PE-Cy7 (clone SB/199)	BioLegend	Cat# 121119
Anti-Mouse CD4 APC (clone GK1.5)	BioLegend	Cat# 100411
*InVivo*MAb Anti-Mouse PD-1 (clone RMP1-14)	BioXCell	Cat# BE0146
Bacterial and virus strains		
NEBstable Competent E. coli	NEB	Cat# C3040H
Endura Electrocompetent cells	Lucigen	Cat# 60242-1
Biological samples		
Healthy donor PBMC buffy coats	New York Blood Center	https://www.nybc.org/
ccRCC Nephrectomy Specimens	Columbia University Irving Medical Center	N/A
Chemicals, peptides, and recombinant proteins		
Recombinant Human IL-2	PeproTech	Cat# 200-02
Recombinant Mouse TPO	PeproTech	Cat# 315-14
Recombinant Mouse SCF	PeproTech	Cat# 250-03
Recombinant Mouse Flt3-L	PeproTech	Cat# 250-31L
Recombinant Mouse IL-7	PeproTech	Cat# 217-17
RetroNectin Recombinant Human Fibronectin	Takara Bio	Cat# T100B
FDA-approved and Investigational Oncology Drug Compound Library	Selleckchem	Cat# N/A (custom)
Gemcitabine (Ly-188011)	Selleckchem	Cat# S1714
Triapine	Selleckchem	Cat# S7470
Floxuridine (NSC 27640)	Selleckchem	Cat# S1299
SYTOX Green Ready Flow Reagent	ThermoFisher Scientific	Cat# R37168
CellTrace Violet Proliferation Kit	ThermoFisher Scientific	Cat# C34557
Ficoll-Paque PLUS (1.077 g/mL)	GE Healthcare	Cat# 17144003
Mitomycin C	Millipore Sigma	Cat# 10107409001
DNase I	Roche/Sigma	Cat# 10104159001
Collagenase D	Roche/Sigma	Cat# 11088866001
LiveDead Fixable Blue Dye	ThermoFisher Scientific	Cat# L34962
BD Brilliant Stain Buffer Plus	BD	Cat# 566385
FoxP3 Fixation/Permeabilization Kit	eBioscience/Thermo	Cat# 00-55214-00
TruStain Monocyte Blocker	BioLegend	Cat# 426103
Fugene HD	Promega	Cat# E2312
RNAseA	Qiagen	Cat# 19101
Biotium EVAGREEN DYE 20X IN WATER 1 ML	Fisher Scientific	Cat# NC0521178
GeneJET Gel Extraction Kit	Fisher Scientific	Cat# FERK0692
Gibson Assembly® Master Mix	NEB	Cat# E2611L
KAPA HiFi HotStart PCR Kit, with dNTPs	Kapa Biosystems	Cat# KK2502
NucleoBond® Xtra Midi EF (50 preps)	Macherey-Nagel	Cat# 740420.50
Puradisc 25 mm PES Syringe Filters	Cytiva	Cat# 6780-2504
RIPA BUFFER	Teknova	Cat# R3792
Phenol:Chloroform:Isoamyl Alcohol (25:24:1, v/v)	Invitrogen	Cat# 15593031
KAPA HiFi HotStart ReadyMix (2X)	Kapa Biosystems	Cat# KK2612
Critical commercial assays		
$CD4^+$ T cell Isolation Kit, Human	Miltenyi Biotec	Cat# 130-096-533
Human Treg Expander DynaBeads	Gibco	Cat# 11129D

(*Continued on next page*)

Continued

REAGENT or RESOURCE	SOURCE	IDENTIFIER
Human Tumor Dissociation Kit	Miltenyi Biotec	Cat# 130-095-929
Mouse Tumor Dissociation Kit	Miltenyi Biotec	Cat# 130-096-730
10x Chromium Next GEM Single Cell 3' Kit v3.1	10x Genomics	Cat# 1000269
Deposited data		
Sorted T-cell Populations RNA-Seq From Patient Blood & Tumor	This Manuscript	https://doi.org/10.17632/vnrsbb4gk9.1
Overexpression Screen Single-Cell RNA-Seq Data	This Manuscript	https://doi.org/10.17632/vnrsbb4gk9.1
Gemcitabine Treatment Single-Cell RNA-Sequencing Data	This Manuscript	https://doi.org/10.17632/vnrsbb4gk9.1
sgRNA counts from CRISPR KO experiment	This Manuscript	https://doi.org/10.17632/vnrsbb4gk9.1
Drug Screen PLATE-Seq Data	This Manuscript	https://doi.org/10.17632/vnrsbb4gk9.1
T-cell ARACNe Network	This Manuscript	https://doi.org/10.17632/vnrsbb4gk9.1
Experimental models: Cell lines		
MC38	Kerafast	Cat# ENH204-FP
MCA205	Millipore Sigma	Cat# SCC173
HEK293T	ATCC	Cat# CRL-11268
Experimental models: Organisms/strains		
Mouse: C57BL/6J	The Jackson Laboratory	Strain# 000664
Mouse: H11-Cas9 (*Igs2*$^{tm1.1(CAG-cas9*)Mmw}$/*J*)	The Jackson Laboratory	Strain# 027650
Mouse: NSG (NOD.Cg-*Prkdc*^{scid} *Il2rg*^{tm1Wjl}/SzJ	The Jackson Laboratory	Strain# 005557
Mouse: Rag1-KO (B6.129S7-*Rag1*^{tm1Mom}/J	The Jackson Laboratory	Strain# 002216
Mouse FoxP3-YFP/Cre (B6.129(Cg)-*Foxp3*$^{tm4(YFP/icre)Ayr}$/J	The Jackson Laboratory	Strain# 016959
Recombinant DNA		
pXPR_053	Addgene	Cat# 113591 (PubMed 30971695)
PsPAX2	Addgene	Cat# 12260 (gift from Didier Trono)
pMD2.G	Addgene	Cat# 12259 (gift from Didier Trono)
Tet-O-FUW-EGFP	Addgene	Cat# 30130 (PubMed 20107439)
Tet-O-FUW-EGFP-P2A-mCherry	This paper	N/A
FUW-M2rtTA	Addgene	Cat# 20342 (PubMed 18786421)
Human CSRNP2 ORF clone	GenScript	Cat# OHu04521
Human TRPS1 ORF clone	GenScript	Cat# OHu21177
Human BANP ORF clone	GenScript	Cat# OHu10822
Human MAFB ORF clone	GenScript	Cat# OHu25119
pFUW-tetO-NR4A3	Addgene	Cat# 139818 (PubMed 30530727)
GFP-FBXL10 (KDM2B)	Addgene	Cat# 126542 (PubMed 29985131)
KLF4 in pENTR223.1	Jussi Taipale lab	PubMed 23332764
STAT4 in pENTR223.1	Jussi Taipale lab	PubMed 23332764
NR4A1 in pENTR223.1	Jussi Taipale lab	PubMed 23332764
EGR1 in pENTR223.1	Jussi Taipale lab	PubMed 23332764
ZEB2 in pENTR223.1	Jussi Taipale lab	PubMed 23332764
EGR3 in pENTR223.1	Jussi Taipale lab	PubMed 23332764
PBX4 in pENTR223.1	Jussi Taipale lab	PubMed 23332764
ID2 in pENTR223.1	Jussi Taipale lab	PubMed 23332764
FOSL2 in pENTR223.1	Jussi Taipale lab	PubMed 23332764
NR3C1 in pENTR223.1	Jussi Taipale lab	PubMed 23332764
GLI1 in pENTR223.1	Jussi Taipale lab	PubMed 23332764
Tet-O-FUW-CSRNP2-P2A-mCherry	This paper	N/A
Tet-O-FUW-TRPS1-P2A-mCherry	This paper	N/A

(*Continued on next page*)

Continued

REAGENT or RESOURCE	SOURCE	IDENTIFIER
Tet-O-FUW-BANP-P2A-mCherry	This paper	N/A
Tet-O-FUW-MAFB-P2A-mCherry	This paper	N/A
Tet-O-FUW-NR4A3-P2A-mCherry	This paper	N/A
Tet-O-FUW-KDM2B-P2A-mCherry	This paper	N/A
Tet-O-FUW-KLF4-P2A-mCherry	This paper	N/A
Tet-O-FUW-STAT4-P2A-mCherry	This paper	N/A
Tet-O-FUW-NR4A1-P2A-mCherry	This paper	N/A
Tet-O-FUW-EGR1-P2A-mCherry	This paper	N/A
Tet-O-FUW-ZEB2-P2A-mCherry	This paper	N/A
Tet-O-FUW-EGR3-P2A-mCherry	This paper	N/A
Tet-O-FUW-PBX4-P2A-mCherry	This paper	N/A
Tet-O-FUW-ID2-P2A-mCherry	This paper	N/A
Tet-O-FUW-FOSL2-P2A-mCherry	This paper	N/A
Tet-O-FUW-NR3C1-P2A-mCherry	This paper	N/A
Tet-O-FUW-GLI1-P2A-mCherry	This paper	N/A
Software and algorithms		
R v3.6.2	N/A	https://cran.r-project.org/bin/macosx/
ARACNe	Basso et al. [20]	http://califano.c2b2.columbia.edu/aracne
VIPER	Alvarez et al.[21]	http://califano.c2b2.columbia.edu/viper
GraphPad Prism v9	GraphPad	https://www.graphpad.com/scientific-software/prism/
FlowJo v10.8.1	BD	https://www.flowjo.com/
Single-Cell VIPER	Obradovic et al.[25]	https://github.com/Aleksobrad/single-cell-rcc-pipeline
Custom Analysis Scripts	This paper	https://doi.org/10.17632/vnrsbb4gk9.1

RESOURCE AVAILABILITY

Lead contact

Requests for further information and reagents should be directed to the lead contact, Dr. Andrea Califano (ac2248@cumc.columbia.edu).

Materials availability

Plasmids from this article will be available from Addgene following publication.

Data and code availability

All data reported on in this manuscript are available in a public Mendeley Data repository at https://doi.org/10.17632/vnrsbb4gk9.1 as of the date of publication, grouped by experiment. VIPER algorithm used for data analysis is publicly available as an R package on Bioconductor and single-cell VIPER helper functions are available as part of previously published workflow on github All original code has been deposited on Mendeley. DOIs in key resources table. Any additional information required to reanalyze the data reported in this paper is available from the lead contact upon request.

EXPERIMENTAL MODEL AND SUBJECT DETAILS

Cell lines

The HEK293T cell line (female) was mycoplasma tested before the lentiviral viral production. Cells were maintained in a 5% CO_2, 95% air, humidified incubator at 37°C, in DMEM supplemented with 1X penicillin-streptomycin and 10% FBS (Sigma, F2442). MC38 colon carcinoma cells (female) were purchased from Kerafast and maintained in a 5% CO_2, 95% air, humidified incubator at 37°C in DMEM supplemented with 10% FBS, 100 U/mL penicillin, and 100 mg/mL streptomycin. MCA205 fibrosarcoma cells (unknown sex) were purchased from Millipore Sigma and maintained in a 5% CO_2, 95% air, humidified incubator at 37°C in RPMI supplemented with 10% FBS, 100 U/mL penicillin, 100 mg/mL streptomycin, 1 mM sodium pyruvate, 100 μM non-essential amino acids, and 0.055 nM 2-mercaptoethanol. MC38 and MCA205 cells utilized in *in vivo* experiments were under 5 passages from purchase.

Primary cell cultures

Human PBMC-derived regulatory T cells were freshly sorted from healthy donor whole buffy coats obtained from the New York Blood Center, or from treatment-naïve clear cell renal cell carcinoma tissues received from patients undergoing standard of care nephrectomy at Columbia University Irving Medical Center. Demographic information relating to donors was kept blinded to researchers, however all donors underwent routine pathogen screening and were found negative. Flow sorted cells were cultured in a 5% CO_2, 95% air, humidified incubator at 37°C in X-VIVO 15 (Lonza) supplemented with 10-500 U/mL recombinant human IL-2 (PeproTech) at a density of 35,000 – 200,000 cells/well in 96-well plates.

Animals

Male and female C57BL/6J (Strain #000664), H11-Cas9 (*Igs2tm1.1[CAG-cas9*]Mmw*/J; Strain #027650), RAG1-KO (B6.129S7-*Rag1tm1Mom/J*; Strain #002216), NSG (NOD.Cg-*Prkdcscid Il2rgtm1Wjl*/SzJ; Strain #005557), and FoxP3$^{YFP/Cre}$ (B6.129(Cg)-*Foxp3$^{tm4(YFP/icre)Ayr}$*/J; Strain #016959) mice were purchased from the Jackson Laboratory (Bar Harbor, ME). Mice were 6-8 weeks old at time of use. All animals were housed and bred in strict accordance with NIH and American Association of Laboratory Animal Care regulations. All experiments and procedures for this study were approved by the Columbia University Medical Center Institutional Animal Care and Use Committee (IACUC).

METHOD DETAILS

Clinical sample collection, sorting, and RNA-sequencing

These methods relate to data as shown in Figure 1. Tissue was collected from treatment-naïve resected tumors across patients with four tumor types, including 8 patients with glioblastoma multiforme, 8 patients with clear cell renal carcinoma, 8 patients with bladder cancer, and 12 patients with prostate cancer (from radical prostastectomies). For prostate cancers, since it can be difficult to identify tumor from freshly sectioned prostatectomies, for each case, prostates were inked and sliced fresh, 8 mm punches were taken, and a thin slice was taken for frozen section to ensure the presence of tumor in adjacent tissues used for cell dissociation and flow cytometry. For each patient, 50ml of peripheral blood was drawn same day as tumor resection. Tumors were dissociated with the GentleMACS OctoDissociator following manufacturer's instruction, and subsequently Tregs and $CD8^+$ T-cells were flow-sorted from tumor along with Tregs, naïve CD4nonTregs, and naïve $CD8^+$ T cells from peripheral blood. An aliquot of flow sorted naïve $CD8^+$ and $CD4^+$ non-Treg were stimulated *ex vivo* with anti-CD3/anti-CD28 beads for 72 hours to induce T-cell activation. Flow-sorted and ex-vivo-stimulated populations were processed to prepare RNA-Seq libraries. RNA-Seq libraries were generated using the Nugen Ovation RNA-Seq System v2 kit (Nugen). Libraries were sequenced on an Illumina HiSeq 2500 with paired end 2 × 100 bp reads. RSEM (v1.2.8–1.2.9) was used with bowtie2 to derive gene-level expression measures, represented as posterior transcripts per million (pmeTPM).

Gene expression and VIPER analysis

Gene Expression was combined across all samples and scaled to log10(Transcripts Per Million + 1). Gene Expression was subsequently scaled across rows by z-score transformation and used as input for Principal Component Analysis (Figure 1B) and differential gene expression.

Log10(TPM+1) matrix was separately used to infer gene regulatory network structure by the ARACNe algorithm. ARACNe was run with 100 bootstrap iterations using 1785 transcription factors (genes annotated in gene ontology molecular function database as GO:0003700, ''transcription factor activity'', or as GO:0003677, ''DNA binding'' and GO:0030528, ''transcription regulator activity'', or as GO:0003677 and GO:0045449, ''regulation of transcription''), 668 transcriptional cofactors (a manually curated list, not overlapping with the transcription factor list, built upon genes annotated as GO:0003712, ''transcription cofactor activity'', or GO:0030528 or GO:0045449), 3455 signaling pathway related genes (annotated in GO biological process database as GO:0007165, ''signal transduction'' and in GO cellular component database as GO:0005622, ''intracellular'' or GO:0005886, ''plasma membrane''), and 3620 surface markers (annotated as GO:0005886 or as GO:0009986, ''cell surface''). ARACNe is only run on these gene sets so as to limit protein activity inference to proteins with biologically meaningful downstream regulatory targets, and we do not apply ARACNe to infer regulatory networks for proteins with no known signaling or transcriptional activity for which protein activity may be difficult to biologically interpret. Parameters were set to zero DPI (Data Processing Inequality) tolerance and MI (Mutual Information) p-value threshold of 10^{-8}, computed by permuting the original dataset as a null model.

Using the ARACNe gene regulatory network structure, VIPER protein activity inference was performed on gene expression signature. First directly on z-score-scaled gene expression signature for all T-cell subtypes, used for Principal Component Analysis and clustering (Figures 1C and 1D). Then separately scaling Tumor and Peripheral Tregs against naïve CD4nonTregs by viperSignature command in Rstudio for comparison of Tumor Treg vs Peripheral Treg (Figure 1E), and scaling all Tregs and CD4nonTregs against naïve $CD8^+$ T-cells by viperSignature for comparison of Tumor Treg vs all Treg and CD4nonTreg controls (Figure 1F).

Random Forest Feature Selection

The full dataset was randomly split into 75% training data and 25% testing data. On training data, a Random Forest Model was built with VIPER-inferred protein activity to classify Tumor Treg vs Peripheral Treg (Figure 1E) or Tumor Treg vs all Controls (Figure 1F), taking the list of all differentially active proteins (t-test p-value < 0.01) as an initial feature set. Features were ranked by mean decrease

in model accuracy and included one-by-one to construct random forest models with feature selection. Predictive power was assessed by Area-Under-ROC-Curve (AUC) in the held-out testing data, and a null model of AUC was constructed from random sampling of the same number of genes (from the set of genes with differential activity p-value = 1.0) 1000 times. For each comparison, the maximum number of discriminative genes was selected for which AUC vs null model remained statistically significant (Figure S2A). These genes are shown in Figures 1C and 1D and aggregated into a combined list of 17 putative Tumor Treg vs Peripheral Treg Master Regulators with Activity specifically upregulated in Tumor Tregs.

CRISPR KO library design

For *in vivo* CRISPR KO screening we designed the target gene list to include 34 genes, which consisted of 17 predicted Tumor Treg MRs, 13 randomly sampled negative control genes (genes with p = 1.0 comparing Tumor Tregs to Peripheral Tregs: In the final analysis, 6 of these genes with negligible baseline expression in Tregs were utilized as true negative controls), Treg context-specific positive controls *Foxp3* and *Cd4*, and core-essential genes *Cdk1* and *Plk1*. All these genes were targeted with 3 sgRNAs. For guide design, we used the Broad Institute Genetic perturbation platform (GPP) sgRNA designer-tool.[73] The guide sequences are found in (Table S1).

CRISPR KO oligo synthesis and library cloning

Oligo libraries (102 oligos) were ordered from Twist-biosciences (Table S1):

From the initial oligo pool, this TREG sub-library was amplified first with KAPA polymerase (KK2502) with the following TREG_1F and TREG_1R PCR primers (see Table S1) and with the following settings:

DNA (oligo pool 1ng/ul) 2ul
5xHF-buffer 5
dNTPs 0.75ul
TREG_1F(10uM) 0.75ul
TREG_1R(10uM) 0.75ul
KAPA pol 0.5ul
SYBR 1.25ul
H2O to 25ul
PCR 1 Protocol:
95C 3min
98C 20s
55C 15s
72C 15s
72C 1min
4C —

The PCR product from PCR1 was gel purified with GeneJet gel purification-kit.

The 2nd PCR prior to the Gibson cloning-step was done with the TREG_2F and TREG_2R primers and the following settings:

DNA (product from 1st PCR) 3ng
5xHF-buffer 5ul
dNTPs 0.75ul
TREG_2F(10uM) 0.75ul
TREG_2R(10uM) 0.75ul
KAPA pol 0.5ul
SYBR 1.25ul
H2O to 25ul
PCR 2 Protocol:
95C 3min
98C 20s
64C 15s
72C 15s
72C 1min
4C —

Both of these amplifications were done with qPCR and the PCR program was stopped before the amplification started to plateau. After PCR the insert was gel purified (GeneJet) and Gibson cloned into BsmBI-digested pXPR_053 (Addgene# 113591). Gibson cloned insert and vector was column purified (GeneJet) and large-scale electroporated into Lucigen Enduro competent cells. The bacterial colonies were scraped from 24,5cm x 24,5cm agar plates, so that the estimated library complexity was > 1000 colonies / sgRNA. Library-plasmid DNA was extracted with NucleoBond Xtra Midi EF-kit (Macherey-Nagel).

Lentiviral packaging of the sgRNA library

13 million HEK293T cells were seeded for each 15cm dish the night before transfection. The following morning, viral transfections were conducted with the following components:

- 22.1ug sgRNA containing pXPR_053 (Addgene 113591).
- 16.6ug PsPAX2 (Addgene 12260)
- 5.5ug PMD2G (Addgene 12259).
- 1660ul of sterile H2O.

After mixing the plasmids and H2O, 110,6ul of Fugene HD (Promega) was added to the mix. The transfection mixture was vortexed, then incubated for 10 minutes before adding dropwise to 293T cells. The transfection mixture was removed the following day and fresh media was added to the cells. Virus was collected at 48h and 72h after initial transfections. To remove cellular debris, the virus-containing supernatant was centrifuged 500 x g for 5min and filtered with 0.45um PES filters (Millipore), followed by ultracentrifugation (25,000rpm for 2h), dissolving the viral pellet into PBS, aliquoting the virus and storing the aliquots at -80C. Viral titer was measured with 293T cells by using FACS and violet-excited GFP in the pXPR_053-plasmid.

sgRNA library transductions into hematopoietic LSK cells

Confirmatory evidence that the predicted proteins regulate tumor Treg infiltration was generated in murine models in a pooled CRISPR KO screen (Figure 2); by comparing the differential representation of Tregs containing MR targeting sgRNAs in tumor versus non-tumor tissue (spleen, as a control).

LSKs from donor Cas9+ mice mice were sorted into 96-well plate (100k LSKs/well) and incubated overnight in SFEM media supplemented with 100 ng/mL of the following cytokines: SCF, TPO, Flt3-Ligand, and IL-7. Pen/Strep was also used in all *in vitro* cultures. The following day, LSK cells were transferred into Retronectin (Takara)-coated 24-well plate and sgRNA library-containing Lentiviruses were added to the wells with MOI 30 (based on viral titering in 293T cells, similarly as in LaFleur et. al, 2019). The final volume was adjusted to 400ul / well by adding cytokine supplemented SFEM stem cell media. The cells were centrifuged at 650 x g for 1.5 hours at 37°C with an acceleration of 2 and a brake of 1. After centrifugation, the plate was placed into 37C incubator for 1h, before adding 500 microliters of prewarmed stem cell media on top of the LSKs followed by overnight incubation. Next day the transduced LSKs were implanted into donor mice irradiated with two doses of 600rads, spaced four hours apart, by intravenous tail vein injection immediately following the second irradiation.

CRISPR validation in chimeric immune editing model

The transduced stem cells were reimplanted into lethally irradiated (6 Gy x2) recipient H11-Cas9 mice in two cohorts (six replicate mice for cohort 1 and three replicate mice for cohort 2), allowing reconstitution of the entire immune system, including Tregs, with a unique pool of MR sgRNAs and control sgRNAs in place. Subsequent subcutaneous implantation of $1x10^6$ MC38 murine colon adenocarcinoma cells allowed direct observation of differential infiltration of tumors by Tregs receiving selected CRISPR guides, in a single, high-throughput experimental screen. For both cohorts, the stem cells were separately implanted and harvested, and Vex^+ sgRNA-bearing Tregs and CD4nonTregs were flow-sorted from Tumor and spleen, separately.

Genomic DNA extraction and preparation of NGS libraries

Since the number of Vex^+ tumor Tregs was very low in any individual mouse and because the mice all share the same genetic background, we decided to pool all tumor Tregs and tumor CD4s together across all mice before the gDNA extraction step in order to reliably purify gDNA with sufficient yield. Before pooling the tumor TREGs or tumor CD4s, the TREG / CD4 cell numbers coming from each individual tumor were carefully counted during FACS sorting.

First the pooled cells (all tumor TREGs or all tumor CD4s) were lysed with 400ul of RIPA-buffer (Teknova) + RNAseA (Qiagen), followed by 1h incubation in 65C. After this, 400ul of Phenol/Chloroform/Isoamyl alcohol (Invitrogen) was added, followed by 6 min centrifugation at room temperature. Finally, the gDNA was recovered by Isopropanol precipitation.

For spleen Tregs and spleen CD4s all the gDNA extractions were done individually for each mouse-sample (not pooled together before the lysis-stage as was done with tumor Tregs and tumor CD4s), since the number of Spleen extracted Vex^+ cells was much higher than with tumor Tregs / tumor CD4s. After the gDNAs of spleen Tregs and spleen CD4s samples were individually purified, spleen Tregs and spleen CD4s gDNAs were pooled before the NGS library prep PCRs. This was done by pooling Spleen Tregs gDNAs and Spleen CD4s gDNAs in the same ratio as earlier Tumor Tregs and Tumor CD4s were pooled prior to gDNA extractions (as measured by Vex^+ FACS cell count).

For the NGS library preparations, the extracted gDNA was split evenly into 8 (for cohort 1) or 4 (for cohort 2) separate technical replicates. Library prep PCRs (2-step PCR protocol with 2 x KAPA Mastermix (KK2612, KAPA Biosystems)) and NGS were done individually to all these technical replicates. Both 1st (with TREG_NGS_1F and TREG_NGS_1R) and the 2nd PCRs (with TREG_NGS_2F

and TREG_NGS_2R) were run in qPCR machine and stopped before amplification started to saturate in order to avoid biases in the library coverage. The following primers and PCR programs were used for the NGS library preps:

1st PCR:	
gDNA	12.5 - 25% of pooled material (depending on the cohort)
2 x KAPA mastermix	12.5ul
TREG_NGS_1F(10uM)	1ul
TREG_NGS_1R(10uM)	1ul
SYBR	1.25ul
H2O	to 25ul

PCR protocol TREGS_NGS_1:	
95C	3min
98C	20s
60C	15s
72C	20s
72C	1min

2nd PCR:	
1:50 diluted DNA template from PCR 1	8ul
2 x KAPA mastermix	12.5ul
TREG_NGS_2F(10uM)	1ul
TREG_NGS_2R(10uM)	1ul
SYBR	1.25ul
H2O	to 25ul

PCR protocol TREGS_NGS_2:	
95C	3min
98C	30s
52.5C	15s
72C	20s
72C	1min

After the 2nd PCR, samples were gel-purified (GenJet), pooled and sequenced with Illumina.

Critically, this experiment would not have been possible on a genome-wide level without initial narrowing of candidate master regulators by VIPER protein activity analysis, due to fundamental limitations in achieving a sufficient number of tumor-infiltrating Tregs harboring guide DNAs for the full set of mouse genes. This is because we typically find fewer than 10,000 tumor-infiltrating Tregs in MC38 tumor model.

Correlation between replicates by gDNA frequency was assessed in each cohort and for each set of replicates following library sequencing (Figure 2D).

In vivo CRISPR KO-screen analysis

Sequencing reads were aligned to a reference of sgRNA template sequences by kallisto to determine a counts matrix of reads per guide for each sample. Differential frequency of guides in Tumor Treg vs Peripheral Treg and Tumor Treg vs Tumor CD4nonTreg was assessed by empiric p-values from normal distribution fitted to a permutation-based null model for each guide (1000 permutations per sgRNA), with Bonferroni correction, and p-values for guides targeting the same gene integrated by Stouffer's Method. P-values across the two replicate experiments were then also integrated by Stouffer's Method (Figures 2F and 2G). For the final analysis 6 /13 of the randomly sampled negative controls with low baseline expression in T cells were ultimately selected as negative controls for the assay. Positive control sgRNAs were significantly depleted post-transduction, indicating successful gene-editing.

CRISPR KO-based tumor growth experiments

Tumor growth was assessed in single-gene CHIME chimeras generated by the CHIME protocol described above. Two unique guide RNAs per gene were pooled to create either Trps1-targeted chimeras (sgTrps1_1 and sgTrps1_2), or non-targeting control chimeras (sgNon-targeting guide 1 and sgNon-targeting guide 2).[30] For sgRNA sequences see Table S1. LSKs were transduced with sgTrps1 or sgControl RNA pools at MOI 50 based on 293T cell line titering. Two cohorts of 5-10 mice were generated, with FACS-sorted Vex^+ (sgRNA-containing) LSK cells from cohort 1 used to generate cohort 2 chimeras.

Due to variability in growth and spontaneous regression of MC38 tumors in these chimeras, mice were subcutaneously implanted with MCA205 (Millipore Sigma). In cohort 1, male and female mice were implanted with $8x10^5$ MCA205 cells on the opposite flank from which spontaneous MC38 regression occurred. In cohort 2, mice were only implanted with $8x10^5$ MCA205. Growth kinetics and survival outcomes were highly reproducible across cohorts. Tumor volumes were measured every 2-3 days by electronic caliper, and mice were euthanized when tumor volume exceeded $1,000mm^3$ or when ulceration exceeded 5mm in diameter. Differential survival between groups was assessed by Kaplan-Meier test. At endpoint, tissues were harvested from cohort 2 mice for downstream assays as described below.

ORF cloning for transcription factor overexpression/reprogramming assay

Full-length open reading frame (ORF) clones for the top 17 predicted TI-TREG-MRs (*EGR1, NR3C1, PBX4, MAFB, ID2, STAT4, NR4A3, NR4A1, TRPS1, EGR3, BANP, ZEB2, KLF4, GLI1, CSRNP2, FOSL2* and *KDM2b*) and *EGFP* (as assay control) were cloned into modified Tet-O-FUW lentiviral expression plasmid (Addgene #30130), which include P2A and mCherry-selection marker. All cloned ORFs were sequence verified. For each ORF-construct we introduced an ORF specific 22nt barcode sequence and 10nt random UMI sequence (see Table S1) located approx. 200 bp upstream of the lentiviral 3'-long terminal repeat (LTR) region of the plasmid. This produces a polyadenylated transcript, which contains the ORF-specific barcode proximal to its 3' end. To increase the 10nt random UMI diversity for each ORF construct, the final step of the cloning procedure (cloning in the ORF specific barcode and ORF UMI into modified Tet-O-FUW (which is already containing all full length ORFs)) was done in pooled fashion with Lucigen Endura competent cells and electroporation for each ORF-construct separately.

For all other cloning-related transformation steps we used NEB Stable competent cells (NEB).

Transcription factor overexpression / reprogramming assay (scRNA-Seq)

All lentiviruses were produced, similarly as with "Lentiviral packaging of the sgRNA library", and viral titers were measured individually for each virus. P-Tregs were collected from healthy donor PBMC. Briefly, healthy donor buffy coats (New York Blood Center) were diluted 1:1 in PBS and layered over ficoll (GE Healthcare; 1.077 g/mL) and spun for 30 min at 400xg with the brake off. PBMC were isolated from the interface and pooled, RBC lysed (ACK buffer; Quality Biological), then washed with PBS. $CD4^+$ T cells were enriched with the Miltenyi $CD4^+$ T cell Isolation kit according to manufacturer's instructions, then stained for flow cytometry sorting with antibodies targeting CD4, CD127, and CD25. Viable Tregs were sorted (Sytox $Green^-CD4^+CD25^+CD127^{lo}$) using a FACSAria II sorter into X-VIVO 15 medium (Lonza) supplemented with 10 U/mL human recombinant IL-2 (PeproTech). Approximately 50k cells were seeded per well in flat-bottom 96-well plates in Treg expansion media (X-VIVO 15 + 500 U/mL human IL-2), and activated with Human Treg Expander beads (Dynabeads; Gibco) according to manufacturer's protocol. The next day, ORF containing lentiviruses were transduced into human P-Tregs by spin-infection (930 x g, 2h, +30C) in arrayed fashion +/- M2RTTA (FUW-M2rtTA, Addgene #20342), a tetracycline-inducible transcriptional amplifier allowing monitoring of MR overexpression at higher and lower levels.[74] The total viral dose for each ORF-virus was optimized to maximize the transduction efficiency for each clone without ill-effects on the TREG viability (data not shown). One day after the transductions, the media was changed and doxycycline (0.5ug/ml) was added to wells in order to activate the M2RTTA-driven tet-promoter. 7 days after the spin-transduction, the arrayed cells were FACS sorted into 2 pools (+M2RTTA and -M2RTTA) in approx. equal cell numbers for each ORF and control. This was followed by 10x chromium run and NGS.

After the Chromium-run, and cDNA amplification, the ORF barcode transcripts were specifically enriched by amplifying with ORF_BC_amplif_oligo_F and ORF_BC_amplif_R-oligos (see Table S1).

This amplified product was spiked in spiked in the final NGS library at 10% total amounts respectively.

High-throughput Treg-directed drug screening

From an initial library of 1,554 FDA-approved or investigational oncology compounds (SelleckChem), single-dose viability screening was performed *in vitro* on human Tregs sorted from buffy coats as described above. 195 compounds were identified which reduced peripheral Treg growth by at least 60% relative to DMSO control at 5uM. For these, dose-response titrations were performed to identify the IC20 dose at which peripheral Treg growth is inhibited by 20%, either by direct toxicity to Tregs or inhibition of Treg cell division. Subsequently, Tumor-Infiltrating Tregs were sorted from a large clear cell renal carcinoma tumor and plated with Treg-expansion beads in culture for 5 days, resulting in $5x10^6$ TI-Tregs. These were suspended at 160,000cells/mL and divided among 2 replicate plates for downstream RNA sequencing (PLATE-Seq) and 1 plate for viability testing in comparison to peripheral Tregs at the P-Treg IC20 dose. Seven drugs with significantly greater toxicity to tumor Tregs vs peripheral Tregs were identified (Figure 3C).

Wells of drug-treated Tregs were RNA-Sequenced and each normalized with viperSignature against the internal DMSO-control wells on the same PLATE. VIPER was run on the normalized gene expression using the T-cell ARACNe network inferred from sorted bulk-RNA-Sequencing clinical data. Drugs were ranked on their overall inversion across patients of the 17-gene Master Regulator

signature previously identified and validated by CRISPR (Figure S3B), as well as on their patient-by-patient inversion of Tumor-Treg vs Peripheral-Treg protein activity signature by OncoTreat (Figure 3E).

Drug-based tumor growth experiments

5-10 female mice per treatment arm were implanted with subcutaneous MC38 (Kerafast) tumor cells. Treatment was initiated after 8-12 days of initial tumor growth when average tumor volume reached 150mm^3 (12 days for C57BL/6J, 10 days for Rag1-KO, 8 days for NSG). Mice were randomized prior to treatment to equalize mean tumor volume and size distribution between groups. Tumors were measured by electronic caliper every 2-3 days, and mice were euthanized when tumor volume exceeded 1000mm^3 or ulceration exceeded a diameter of 5mm. Gemcitabine was administered IP in 100ul sterile PBS for 3 total doses (q3D) at indicated dose. Floxuridine and triapine were injected IP daily for 9 doses at 1mg/kg and 5mg/kg, respectively. Mice received 200ug anti-PD-1 (RMP1-14; BioXCell) IP in sterile PBS for 3 total doses (q3D). Treatment response outcomes were assessed by cox proportional hazards model, Kaplan-Meier curve, and computation of mean tumor growth slope over time. Tumor growth curves display the average tumor volume over time with standard deviation represented by error bars or shading, with each average growth curve terminating when the first animal in each treatment condition reached end stage.

In vitro Treg suppression assay

At tumor growth endpoint, spleens from Trps1-targeted CHIME chimeras were harvested, dissociated into single cell suspensions, RBC lysed, removed of B cells (Miltenyi CD19$^+$ Microbeads; per manufacturer's protocol), and frozen in 90% FBS + 10% DMSO. Later, cells were thawed and rested overnight in T cell media (RPMI + 10% FBS + 100U/mL penicillin + 100mg/mL streptomycin + 1mL sodium pyruvate + 100uM non-essential amino acids + 5mM HEPES + 0.055nM 2-mercaptoethanol) at 2x106 cells/mL. Tregs were flow sorted on a BD FACSAria II cytometer (Sytox Green$^-$CD3$^+$CD4$^+$CD25$^+$), and Tregs containing Trps1-sgRNAs were separated from non-perturbed Trps1-WT Tregs by Vex fluorescence.

Spleens from naive C57BL/6J mice were harvested to isolate responder T cells and APCs for the suppression assay. Briefly, spleens were mechanically mashed through a 70um filter, RBC lysed, and resuspended in MACS buffer (PBS + 0.5% BSA + 2mM EDTA). Splenocytes were split in half for CD4 T cell isolation (Miltenyi mouse CD4$^+$ T cell isolation kit) and APC enrichment (Miltenyi CD3$^+$ microbeads) according to manufacturer's protocols. APCs were fixed by incubation with 25ug/mL mitomycin C (Millipore Sigma) in T cell media for 30 min at 37o C. CD4$^+$ T cells were stained with 10uM CellTrace Violet in 1mL T cell media for 5 min at room temperature protected from light. For the assay, Tregs containing Trps1-sgRNAs and Trps1-WT Tregs were serially diluted in triplicate, targeting 20k Tregs for the 1:1 ratio wells. 20k CTV+ CD4$^+$ responder T cells were added to all wells, then 20k fixed APCs were added, followed by soluble anti-CD3 antibody (clone 145-2C11; BioLegend; final concentration of 1ug/mL). Cells were incubated at 37o C for ~80 hours, then CTV dilution was assayed in responder CD4$^+$ T cells using a Cytek Aurora full spectrum flow cytometer.

Histology

At endpoint, shaved skin, colon, small intestine, liver, and kidney tissues were harvested from TRPS1-targeted and Scrambled control CHIME chimeras. Intestinal organs were flushed with PBS. All tissues were fixed in 15mL 10% formalin for 24-36 hours, then were transferred to 70% ethanol before routine FFPE embedding, slide sectioning, and H&E staining at the Columbia Molecular Pathology Shared Resource core. Tissue slides were scanned up to 40X magnification and imaged in QuPath-0.3.2. Pathology scores were provided by independent expert pathologist review, blinded to sample group status.

High dimensional spectral flow cytometry immune profiling

Tumors and spleens were collected from 12-day MC38 tumor bearing mice 24, 48, or 72 hours post treatment with Gemcitabine (120mg/kg, 12mg/kg, or 3mg/kg; 5-10 mice per group per time point). Tumors and spleens were minced and digested by 30 min incubation with shaking at 37^o in X-VIVO 15 media containing 0.16ug/mL DNaseI (Roche) and 1mg/mL Collagenase D (Roche). Digest reactions were quenched by addition of RPMI + 10%FBS and vortexing for 30 seconds. Spleen samples were RBC lysed in 1mL ACK buffer for 1-2 minutes, followed by quenching with 9mL RPMI + 10%FBS. Samples and cells for single stain controls were plated in U bottom 96-well plates, then were washed with PBS followed by staining with LiveDead Fixable Blue dye (ThermoFisher) for 30 minutes at room temperature on a shaker. Cells were washed, blocked with Tru-Stain anti-mouse FcX Plus (BioLegend), then stained with surface marker antibodies supplemented with BD Brilliant Stain buffer and TruStain Monocyte Blocker (BioLegend) for 30 minutes at room temperature on a shaker. Samples were washed, then fixed and permeabilized using the FoxP3 Fixation kit (eBioscience) for 30 minutes at room temperature on a shaker. Cells were washed in 1X PermWash (eBioscience) then stained with intracellular antibodies in 1X PermWash overnight at 40 C on a shaker. Cells were then washed with 1X PermWash and FACS buffer then acquired on a 5-laser Cytek Aurora full spectrum flow cytometer. High dimensional data analysis was completed in FlowJo v10.8.1 (BD) using UMAP v3.1 and FlowSOM v3.0.18 plugins downloaded from FlowJo Exchange.

Single-cell RNA-seq profiling of gemcitabine effect on TI-Tregs

To test the hypothesis that low-dose Gem modulates TI-Tregs, we performed single cell RNA sequencing of MC38 tumor- and spleen-derived Tregs 24 hours after exposure to a single dose of 12 mg/kg Gem as well as 24 hours after vehicle control. For this study, we implanted *FoxP3$^{Yfp\text{-}Cre}$* mice with 1x10^6 MC38 subcutaneously to facilitate flow-sorting of TCR-β^+ CD4$^+$ FoxP3$^+$ Tregs from tumor and spleen specifically by the YFP marker. Tissue was harvested at day 14 post tumor-implantation, and fresh tissue

was minced to 2-4 mm sized pieces in a 6-cm dish and subsequently digested to single cell suspension using Mouse Tumor Dissociation Kit (Miltenyi Biotec) and a gentleMACS OctoDissociator (Miltenyi Biotec) according to the manufacturer's instructions.

Dissociated cells were flow-sorted for YFP^+ Tregs and processed for single-cell gene expression capture (scRNASeq) using the 10X Chromium 3' Library and Gel Bead Kit (10x Genomics), following the manufacturer's user guide at the Columbia University Genome Center. After GelBead in-Emulsion reverse transcription (GEM-RT) reaction, 12-15 cycles of polymerase chain reaction (PCR) amplification were performed to obtain cDNAs used for RNA-seq library generation. Libraries were prepared following the manufacturer's user guide and sequenced on Illumina NovaSeq 6000 Sequencing System. Single-cell RNASeq data were processed with Cell Ranger software at the Columbia University Single Cell Analysis Core. Illumina base call files were converted to FASTQ files with the command "cellranger mkfastq." Expression data were processed with "cellranger count" on pre-built mouse reference. Cell Ranger performed default filtering for quality control, and produced a barcodes.tsv, genes.tsv, and matrix.mts file containing transcript counts for each cell, such that expression of each gene is in terms of the number of unique molecular identifiers (UMIs) tagged to cDNA molecules corresponding to that gene.

These data were loaded into the R version 3.6.1 programming environment, where the publicly available Seurat package was used to further quality-control filter cells to those with fewer than 25% mitochondrial RNA content, more than 1,000 unique UMI counts, and fewer than 15,000 unique UMI counts. Pooled distribution of UMI counts, unique gene counts, and percentage of mitochondrial DNA after QC-filtering is shown in Figure S5A. Gene Expression UMI count matrix was processed in R using the Seurat SCTransform command followed by Seurat Anchor-Integration. The sample was clustered on gene expression by a Resolution-Optimized Louvain Algorithm.[25,75] Protein activity was inferred for all cells by VIPER using the SCTransform gene expression signature and the T-cell ARACNe network derived from sorted T-cell bulk-RNA-Seq. The single-cell data were then re-clustered on VIPER protein activity (Figure S5B). Top 5 most differentially upregulated proteins per cluster were assessed by t-test (Figure S5C). Enrichment of the TI-Treg MRs was assessed by Gene Set Enrichment Analysis (GSEA) on a cell-by-cell basis, with normalized enrichment scores shown in Figure 5E and protein activity of the individual MRs shown in Figure 5D. Cluster frequencies were plotted for each sample (Vehicle-Treated Tumor, Vehicle-Treated Spleen, Gem-Treated Tumor, Gem-Treated Spleen), with pairwise comparisons in frequency assessed by Fisher's Exact test and cox proportional hazards model (Figure 5G).

QUANTIFICATION AND STATISTICAL ANALYSIS

All analyses and statistics were performed in R version 3.6.2 or GraphPad Prism v9. P-values were considered statistically significant at less than 0.05, with multiple testing correction by Benjamini-Hochberg method where appropriate. All data are available in a Mendeley Data repository (Reserved https://doi.org/10.17632/vnrsbb4gk9.1).